Applied Energy 380 (2025) 125120

Contents lists available at ScienceDirect

Applied Energy

journal homepage: www.elsevier.com/locate/apenergy

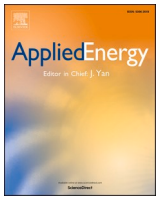

Nature-inspired innovative platform designs for optimized performance of Floating vertical Axis wind turbines

Qingsong Liu [a], Musa Bashir [a,*], Haoda Huang [b], Weipao Miao [b], Zifei Xu [a], Minnan Yue [b], Chun Li [b]

[a] School of Engineering, University of Liverpool, The Quadrangle, Brownlow Hill, L69 3GH, United Kingdom
[b] School of Energy and Power Engineering, University of Shanghai for Science and Technology, Shanghai, 200093. PR China

HIGHLIGHTS

- A nature-inspired platform is proposed to optimize floating VAWT performance.
- A parametric modeling framework for biomimetic structures is developed.
- The underlying mechanism for mitigating power output fluctuations is identified.
- Results show a 10 % reduction in the standard deviation of the power coefficient curve.
- The platform's rotational energy is reduced by 32 %, improving surge and pitch stability.

ARTICLE INFO

Keywords:
Floating VAWT
Computational fluid dynamics
Nature-inspired
Platform stability

ABSTRACT

Floating vertical axis wind turbines (VAWTs) experience load transients during each rotation, even under stable wind conditions. These transients are further intensified by platform motion, affecting the stability of power output. In this study, a biomimetic floating platform inspired by the *Victoria Amazonica* (VA) is proposed to mitigate power output fluctuations by enhancing platform stability. The research focuses on an H-type floating VAWT mounted on the OC4 semi-submersible platform, using a dynamic fluid-body interaction (DFBI) approach coupled with volume of fluid (VOF) multiphase flow model to simulate aero-hydro dynamics. First, a parameterized model of VA leaf venation is developed using an Iterated Function System (IFS), combined with topology and size optimization to generate different VA configurations with varying branch levels (VAS, VAM, VAL). Subsequently, the hydrodynamic performance of the individual platform incorporating these VA configurations is evaluated. Results show that this nature-inspired design significantly reduces the platform's surge, heave, and pitch responses by enhancing the vortex capture capability of the lower pontoons, which dissipates kinetic energy and increases damping. The effectiveness of this novel design improves as the VA branch levels increase. Finally, the impact of the VAL on the aero-hydro coupling performance of the integrated floating VAWT system is further investigated. The VAL configuration effectively reduces the power coefficient fluctuation and decreases the standard deviation by approximately 10 %, primarily by minimizing platform translation and rotation responses. This reduction lessens the interaction between the blades and the incoming flow, resulting in a more stable power output. These findings contribute to the optimization of floating VAWT designs, improve technology readiness levels (TRL), and strengthen confidence in the Floating VAWT concept for industrial-scale deployment in deep waters.

1. Introduction

In the past five years, the global wind power capacity has increased by 443.9 GW, accounting for 42 % of the current total installed capacity (1021 GW) [1]. Although offshore wind power constitutes a smaller share, it has attracted more attention in mature markets due to the increasing geographical constraints on fixed wind farms. By the end of 2023, the total global installed offshore wind capacity reached 75.2 GW [2] and is expected to reach 138 GW between 2024 and 2028, positioning offshore wind as a new engine for economic growth.

* Corresponding author.

https://doi.org/10.1016/j.apenergy.2024.125120
Received 24 September 2024; Received in revised form 15 November 2024; Accepted 7 December 2024
Available online 13 December 2024

At present, horizontal axis wind turbines (HAWTs) dominate offshore wind power generation due to their high efficiency and extensive commercialization [3]. Offshore HAWTs are typically installed on fixed-bottom support structures (Fig. 1 a-b), such as gravity base or monopile foundations for depths around 30 m and jacket foundations for depths around 50 m [4]. However, about 80 % of the world's high-quality offshore wind potential is in deep waters over 60 m in depth [5,6], where the advantages include high wind speeds, stable wind directions, high energy density, low wind shear, and low turbulence [7]. With ongoing advancements in wind power technology, deep-sea wind energy is showing great application potential. Drawing on experiences from the offshore oil and gas industry, floating wind power technology addresses the limitations of fixed platforms, offering new opportunities to exploit deep-sea wind resources. Various floating platform designs, combined with different mooring systems, such as Spar [8], Semi-Submersible [9], and Tension Leg Platform (TLP) [10], have been widely researched and explored, as shown in Fig. 1 c-e.

1.1. The renaissance of Floating VAWTs

As the size of wind turbine blades increases, the design and deployment costs of HAWTs rise correspondingly, primarily due to the added weight of heavy machinery mounted at the top of the tower, such as generators, gearboxes, and control systems, which introduce substantial structural challenges. For example, General Electric (GE) has launched the Hailade-X 12 MW offshore wind turbine [12], featuring a nacelle height of 207 m and a total weight of 675 tons. In deep-sea operations, this turbine generates significant overturning moments, necessitating large floating foundations and specialized ballast systems for stability, further driving up installation and commissioning costs. According to a 2022 assessment by the National Renewable Energy Laboratory (NREL) on 12 MW offshore HAWTs [13], the levelized cost of electricity (LCOE) for fixed-bottom and floating systems was $95/MWh and $145/MWh, respectively, with the floating system costing 52.6 % more. This highlights the substantial cost increase associated with floating HAWTs as they continue to scale up in size.

Floating vertical axis wind turbines (VAWTs) are emerging as a promising option for deep-sea wind energy due to their advantages in power density, directionality, and simplicity in operations and maintenance (O&M) [14–16]. In the 1980s, the U.S.-based FloWind Corporation launched commercial VAWT projects [17], installing more than 500 two-blade Φ-type VAWTs in California's Altamont and Tehachapi Passes. However, frequent failures in the extruded aluminum alloy blades led to the catastrophic collapse of a FloWind-19 VAWT in 1986 due to blade fatigue. Additionally, early projects lacked precise calculations of VAWT power curves and wake losses, leading to significantly lower-than-expected power generation. As a result, VAWTs struggled to compete with HAWTs in the market, causing the technology's development to stall for nearly two decades. In the mid-2000s, renewed interest in large-scale VAWT research arose, driven by the technical challenges facing HAWTs and rising energy costs. Advances in wind energy technology, particularly the introduction and application of high-performance composite materials [18], improved understanding of fatigue loads, and the development of advanced control strategies, addressed many of the issues that had previously hindered VAWT development. As wind farms moved into deeper waters, research teams and institutions proposed numerous innovative floating VAWT concepts between 2007 and 2016, including DeepWind [19,20], VertiWind [21,22], Gwind [23], Aerogenerator X [24,25], Skwid [26], SeaTwirl-S1 [27], and TwinFloat [28]. However, none of these concepts successfully reached commercial deployment.

Recently, SeaTwirl secured a concession for waters near Bokn, Norway, with plans to install the world's first 1 MW floating VAWT [29]. The prototype stands approximately 135 m tall, with an 80 m Spar floating platform submerged beneath the water. The launch of this project marks a significant milestone for offshore VAWT development, representing a key breakthrough toward commercial deployment.

1.2. Overview of enhancing platform stability

Despite extensive design and research efforts dedicated to floating VAWTs, they still face competition from HAWTs, which have benefited from decades of experience with offshore fixed wind projects and are technologically more advanced. Currently, the largest operational floating VAWT prototype connected to the grid, the SeaTwirl-S1, has a power output of only 30 kW, far below the scale required for deep-sea applications. This highlights a significant gap between the current capacity of the technology and its commercial viability. Therefore, fundamental research into large MW-scale floating VAWTs is essential to advance the technology readiness level (TRL).

The primary technical challenges facing VAWTs arise from their aerodynamic efficiency and structural integrity. Studies have shown that, under identical inflow conditions, VAWTs experience greater fluctuations in aerodynamic loads compared to HAWTs [30], which are further intensified by the platform motion [31], ultimately affecting grid integration and stability. Reducing platform dynamic responses can mitigate these issues, lower structural fatigue, and enhance resistance to extreme wave loads, thereby reducing manufacturing and O&M costs. Consequently, research on platform modifications and stability improvements for floating wind turbines has become a focal area of scholarly interest.

For instance, several novel floating platform designs have been

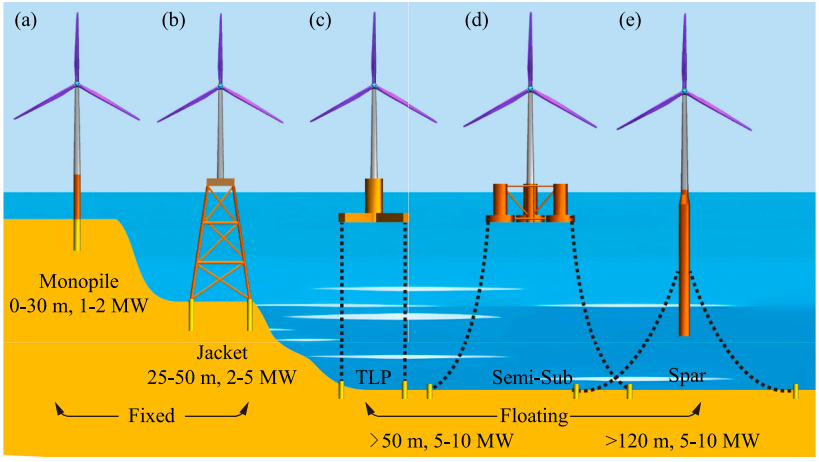

Fig. 1. Comparison of different offshore HAWT platform [11].

developed to address specific offshore wind turbine requirements. Han et al. [32] proposed a Submerged Tension Leg Platform (STLP) suitable for medium water depths (70–150 m). This design enables stable offshore towing without the need for additional stabilization measures, significantly reducing transportation and installation costs. Zhang et al. [33] introduced a novel semi-submersible platform with slanted side columns, comparing it with the OC4 (Offshore Code Comparison Collaboration Continuation, Phase IV) semi-submersible platform. They analyzed the hydrodynamic response under coupled wind, wave, and current conditions for varying wave angles and frequencies. The results showed that the new platform exhibited superior recovery capability under external loads compared to the OC4 platform. Additionally, it significantly reduced the peak heave response, effectively lowering the risk of resonance in the heave direction. Bashetty et al. [34] proposed three floating platforms designed to support multiple HAWTs, employing CFD methods to calculate the wake interference effects of different layouts. They found that the pentagonal platform layout exhibited improved wake velocity distribution. However, hydrodynamic frequency-domain analysis indicated that pitch and heave responses were notably higher than other degrees of freedom for the same layout. Shen et al. [35] modified the triangular semi-submersible platform design of the Fuyao floating HAWT and proposed a V-shaped floating platform. Through fully coupled simulations between NREL FAST and ANSYS AQWA using a Dynamic Link Library (DLL) for time-domain analysis (F2A [36]), results showed that compared to the original triangular platform, the V-shaped design reduced pitch and yaw motions by 40.4 % and 12.9 %, respectively, and also lowered maximum mooring line tension by 17.4 %. Ding et al. [37] proposed the concept of a 3 × 3 array Spar platform, linking nine floating HAWTs through a shared mooring system. ANSYS AQWA was used to analyze the dynamic response under different sea conditions. The results demonstrated that the array layout resulted in smaller sway responses compared to individual floating HAWTs under normal sea conditions, with increased sway only at the four corner platforms. In extreme sea conditions, each floating HAWT in the array exhibited excellent pitch stability.

In addition to new platform designs, researchers have also focused on improving the stability of existing platforms by incorporating damping structures. Ding et al. [38] proposed the installation of helical strakes on a Spar platform to study their impact on the dynamic response of floating HAWTs. Using orthogonal experimental design, they assessed the influence of the number, height, and pitch ratio of the helical strake on platform dynamics. Results showed that when the number of strakes was two, with a vertical height of 0.15 times the platform diameter, and a pitch ratio of 5, the platform's stability in both heave and pitch was significantly improved. Yang et al. [39] investigated a novel motion-stabilizing device consisting of multiple heave plates. Experimental and numerical results demonstrated that, when connected to the bottom of a Spar platform via arms, this device could use the damping force generated by its surfaces to stabilize the floating HAWT. Compared to traditional heave plates, the new stabilizing device significantly improved system stability within a wave period range of 1.5 to 4 s. Yue et al. [40] studied the impact of heave plate installation positions on the hydrodynamic performance of a floating HAWT, based on the OC3 Spar platform, under coupled wind and wave conditions. The study showed that while different installation positions effectively suppressed heave response, they had little effect on surge. Notably, placing the heave plates near the upper part of the Spar platform greatly reduced pitch effects. Yao et al. [41] modified the OC3 Spar platform by adding porous structures near the waterline and investigated the platform's dynamic response over a wave period range of 5 to 22 s. The results revealed that introducing porous structures significantly increased the platform's added mass and radiation damping, leading to a reduction in surge, pitch, and heave responses by approximately 2 %, 7 %, and 22 %, respectively. In particular, the heave response was reduced by 16 % to 77 %.

Further research has focused on optimizing platform stability through closed-loop control algorithms. Wakui et al. [42] developed a predictive control model for floating HAWTs. By considering wave height and incoming wind speed as forecasted disturbance factors, they conducted coupled aero-elastic-hydro-control simulations on a 5 MW floating HAWT. The results showed that the proposed predictive control model significantly improved power output and platform stability under extreme wind speeds, while also reducing dynamic loads on the supporting components.

1.3. Research motivation and main work

The majority of current research on floating wind turbine platforms has concentrated on three primary areas: the development of new platform designs, the addition of damping structures to existing platforms, and the use of closed-loop control algorithms to enhance platform stability. However, these efforts have largely focused on HAWTs, with relatively few studies addressing the unique challenges associated with floating VAWTs. Although several conceptual designs for floating VAWT platforms have been introduced, these designs remain largely proprietary, with limited public access to detailed research methods, platform attributes, and performance data. This lack of transparency hinders the ability to assess and refine these platforms. Moreover, the rotational dynamics of VAWTs introduce unique challenges, such as the potential for gyroscopic effects to exacerbate pitching motions. Therefore, work still needed to develop floating platforms tailored to unique aerodynamic performance of floating VAWT.

The leaves of the giant *Victoria Amazonica* (VA) are one of nature's outstanding engineering feats, and significant progress has been made in understanding the mechanical functions they embody [43]. The VA, native to the equatorial Amazon Basin, has a bottom surface covered with lattice-like veins that radiate outward from its petiolar attachment, extending into multiple layers of radial branches, as shown in Fig. 2. Perpendicular to these branches are concentrically arranged ribs, dividing the underside of the VA leaf into irregular quadrilateral chambers.

The VA's main veins, branches, and ribs work together to support the weight of the giant leaf while forming air-filled compartments that enhance buoyancy. This design balances mechanical strength with lightweight properties, offering excellent load-bearing capability and hydrodynamic performance, which has inspired artists, engineers, and architects for centuries. A classic example (Fig. 3) is the support structure of the Crystal Palace in Victorian London [44], designed by Joseph Paxton, an 18-acre glass and iron structure completed in 1851 and destroyed by fire 85 years later, which was inspired by the vein structure of the VA.

In this paper, a novel floating platform inspired by the vascular architecture of VA is designed to explore its effectiveness in improving the power output stability of floating VAWT. The outline of this paper is as follows: Section 2 introduces the methodology and the process of VA parametric modeling; Section 3 describes the geometric model of the floating VAWT and the nature-inspired platform; Section 4 focuses on the developed numerical model and validation approach; Section 5 presents the results and analysis; and Section 6 concludes with the main findings of the study.

2. Methodology

The floating VAWT operates in a complex multi-physics marine environment, characterized by aero-hydro-multibody dynamics, which poses significant challenges for performance optimization and analysis. In this study, an unsteady computational fluid dynamics (CFD) approach is employed to simulate the aerodynamic and hydrodynamic responses, fully accounting for physical phenomena such as fluid viscosity, wave diffraction, and radiation effects. The Dynamic Fluid-Body Interaction (DFBI) module in STAR-CCM+ is used to compute the six degrees of freedom (six-DOF) motion of a full-scale floating VAWT model,

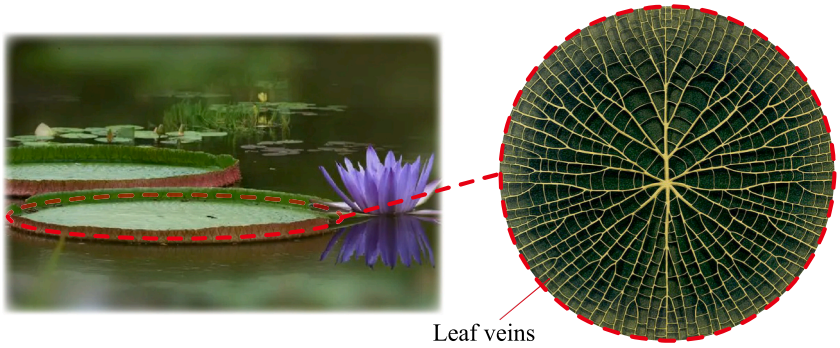

Fig. 2. Giant VA plant and its leaf venation structure.

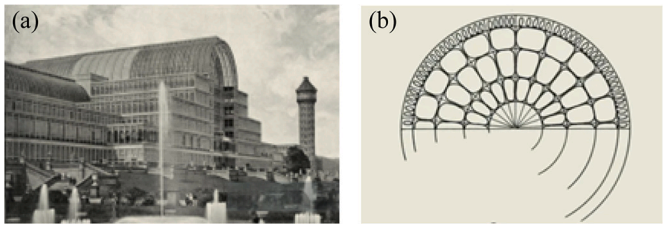

Fig. 3. Application of VA structure in architecture: (a) The Crystal Palace, London[45], (b) Sketch of VA[46].

including rotating blades, the tower, platform, and mooring system. The Volume of Fluid (VOF) multiphase flow model is applied to capture the fluid-induced dynamic motion in the air-water multiphase flow environment.

2.1. DFBI module

The coupling between the fluid and a six-DOF rigid body is referred to as Dynamic Fluid-Body Interaction (DFBI). In the absence of physical constraints, the rigid body is free to move in any direction, and its dynamic behavior is simulated by solving the translational and rotational equations of motion for the body's center of mass. In the global coordinate system, the translational equation of motion for the center of mass is expressed as follows [47]:

$$m\,d\mathbf{v}/dt = \mathbf{f} \tag{1}$$

where m represents the mass of the rigid body, $\mathbf{f}$denotes the total external force acting on the rigid body, and $\mathbf{v}$is the velocity of the center of mass.

The rotation of the rigid body is expressed in the local coordinate system of the body's center of mass, defined as follows [48]:

$$\mathbf{M}\,d\boldsymbol{\omega}/dt + \boldsymbol{\omega} \times \mathbf{M}\boldsymbol{\omega} = \mathbf{n} \tag{2}$$

$$\mathbf{M} = \begin{pmatrix} M_{xx} & M_{xy} & M_{xz} \\ M_{xy} & M_{yy} & M_{yz} \\ M_{xz} & M_{yz} & M_{zz} \end{pmatrix} \tag{3}$$

where $\boldsymbol{\omega}$represents the angular velocity, $\mathbf{n}$denotes the total moment acting on the rigid body, and$\mathbf{M}$ is the moment of inertia tensor. Due to the symmetry of the tensor, it can be defined by two components: the principal moments of inertia $(M_{xx}, M_{yy}, M_{zz})$and the products of inertia(M_{xy}, M_{xz}, M_{yz}).

2.2. VOF multiphase model

The VOF multiphase model is primarily used in CFD simulations to predict the behavior and interaction of immiscible fluids, particularly in scenarios involving sharp phase interfaces. This model is especially effective at tracking and simulating complex multiphase flows with clearly defined boundaries between phases. The distribution of each phase and the position of the interfaces are described by the volume fraction function α_i as follows:

$$\alpha_i = V_i/V \tag{4}$$

where V_i represents the volume of phase i within the computational cell, and V denotes the total volume of the cell. The sum of the volume fractions of all phases within the cell must equal 1. This study considers only two-phase flow, air and water, hence the condition $\alpha_{air} + \alpha_{water} = 1$ is satisfied. The mass conservation equation for phase i is expressed as follows [49]:

$$\frac{\partial}{\partial t}\int_V \alpha_i dV + \oint_A \alpha_i \mathbf{v}\cdot d\mathbf{a} = \int_V \left(S_{\alpha_i} - \frac{\alpha_i}{\rho_i}\frac{D_{\rho_i}}{Dt}\right) dV - \int_V \frac{1}{\rho_i}\nabla\cdot(\alpha_i \rho_i \mathbf{v}_{d,i})\, dV \tag{5}$$

where $\mathbf{a}$ represents the surface area vector, $\mathbf{v}$ is the velocity of the mixture (mass-averaged), $\mathbf{v}_{d,i}$ denotes the diffusion velocity of phase$i$, $S_{\alpha_i}$is the user-defined source term for phase i, and $D_{\rho i}/Dt$ is the material derivative of the density$\rho_i$of phase$i$.

The VOF wave model in STAR-CCM+ is employed to simulate surface gravity waves at the air-water interface, using a fifth-order approximation based on Stokes wave theory to model regular waves. The fifth-order VOF wave is derived from Fenton's theory [50], which allows for a more detailed representation of wave profiles and the complex relationships between phase velocity, water depth, wave height, and wave current velocity. This high-order approximation enables the model to more accurately simulate wave propagation characteristics and their interactions with floating platforms, leading to precise predictions of the hydrodynamic response of floating VAWTs.

To quantify the nonlinearity of the waves, the dimensionless Ursell number U_R[51] is introduced , which is defined as follows:

$$U_R = H\lambda^2/d^3 \tag{6}$$

where H represents the wave height, λ is the wavelength, and d is the water depth. The fifth-order VOF wave model is applicable only when U_R is less than 30.

Additionally, to prevent wave reflection at the outlet boundary from affecting the floating platform, a wave damping mechanism can be introduced. This wave damping effectively reduces the vertical motion of the waves by adding a resistance term to the vertical velocity component, thereby minimizing the potential for wave reflection. Following the method proposed by Choi and Yoon [52], STAR-CCM+ incorporates a damping term in the equation for the vertical velocity (δ) as follows:

$$S_z^{\mathrm{d}} = \rho(f_1 + f_2|\delta|)\frac{e^{\kappa} - 1}{e^{1} - 1}\delta \tag{7}$$

$$\kappa = \left(\frac{x - x_{sd}}{x_{ed} - x_{sd}}\right)^{n_d} \tag{8}$$

where x_{sd}represents the starting point of the damping region in the x-direction during wave propagation, and x_{ed} denotes the end point of the wave damping boundary. The parameters f_1, f_2 and n_d are the damping model coefficients, and δ is the vertical velocity component.

2.3. Catenary coupling model

In STAR-CCM+, the catenary coupling model is capable of simulating elastic, quasi-static catenaries or mooring lines. The catenary is suspended between two endpoints and is influenced by its own weight in a gravitational field, as illustrated in Fig. 4.

The curve shape of the catenary in a state of force equilibrium is defined as follows [53]:

$$x = ap + bsinh(p) + \lambda \tag{9}$$

$$y = acosh(p) + bsinh^2(p)/2 + \eta \tag{10}$$

$$p_1 \le p \le p_2 \tag{11}$$

where p is the variable in the parametric equation, varying within the given range$[p_1, p_2]$, p_1 and p_2 represent the positions of the fixed point a_1 and the guide point a_2 of the catenary, respectively. The constantsλ and η are integration constants, related to the positions of the two endpoints of the catenary and its total mass. The constants a, $b$and c are defined as follows:

$$a = c/\lambda_m g \tag{12}$$

$$b = ca/K_c L_r \tag{13}$$

$$c = \lambda_m L_r g/(sinh(p_2) - sinh(p_1)) \tag{14}$$

where g represents the acceleration due to gravity, λ_m is the mass per unit length of the catenary,L_r is the length of the catenary in its relaxed state; and K_c is the stiffness. The directions of the forces F_1 and F_2 acting at the two ends of the catenary correspond to the local tangential directions of the catenary at endpoints a_1 and a_2, respectively. These expressions reflect the tensile forces experienced by the catenary at its endpoints, with their directions aligned with the tangent of the catenary curve at those points.

$$F_{1,x} = c \tag{15}$$

$$F_{1,y} = csinh(m_1) \tag{16}$$

$$F_{2,x} = -c \tag{17}$$

$$F_{2,y} = -csinh(m_2) \tag{18}$$

2.4. Parametric modeling of VA leaf venations

The VA leaf venations exhibit random fractal-like geometric characteristics [43, [54]]. A parametric model of the VA vascular architecture, including the main veins, branches, and ribs, was constructed in the Grasshopper visual programming environment within the Rhino software [55]. The modeling process began with a series of concentric circles, establishing the primary structure of the leaf venation. Radial lines were then added to simulate the branching pattern of the leaf veins, and additional subdivisions were introduced iteratively to refine the network, creating a realistic representation of the complex vein structure. Using the voxel manipulation functions in the Grasshopper plugin Dendro, the shape and dimensions of the leaf vein curves were optimized. This optimized model, as shown in Fig. 5, was then applied to the bottom of the pontoons in the semi-submersible floating platform, enhancing the stability of the floating VAWT system.

The parametric modeling process for VA leaf venations is as follows: i. A series of parameterized concentric circles is created as the basic framework of the VA leaf venations, with the radius of each circle increasing incrementally according to a predefined step. ii. The number of points on each concentric circle is determined using the iterative function $n_x = y \bullet x \bullet 2–2$, where x is the index of the concentric circle and y is a constant set to 5. iii. Points are generated randomly or pseudo-randomly on each concentric circle to simulate the natural growth patterns of the VA leaf venation branches. iv. A graph theory algorithm is used to compute the shortest paths between points on different circles, generating a connected network of curves. v. The concentric circles used during the construction are removed, leaving the leaf venation network intact. vi. The curve smoothing algorithm (Chaikin) is applied to the edges of the leaf venation network to perform corner cutting and smoothing, enhancing visual continuity and a natural appearance.

Fig. 6 shows the construction of the VA vein structure by increasing the number of concentric circles and branching levels. Starting with a few circles and simple branches, the model gradually adds complexity, resulting in a more intricate vein network. This approach effectively mimics the natural fractal pattern of the VA leaf venations, providing a biomimetic basis for optimizing platform pontoon design.

A 10-level branching structure was selected to initialize the modeling of the VA leaf venations, with rib structures constructed at equal intervals around the concentric circles. To capture the characteristics of the random fractal structure, the shape and size of the original vein branching structure were optimized, resulting in the final VA parametric model, as shown in Fig. 7.

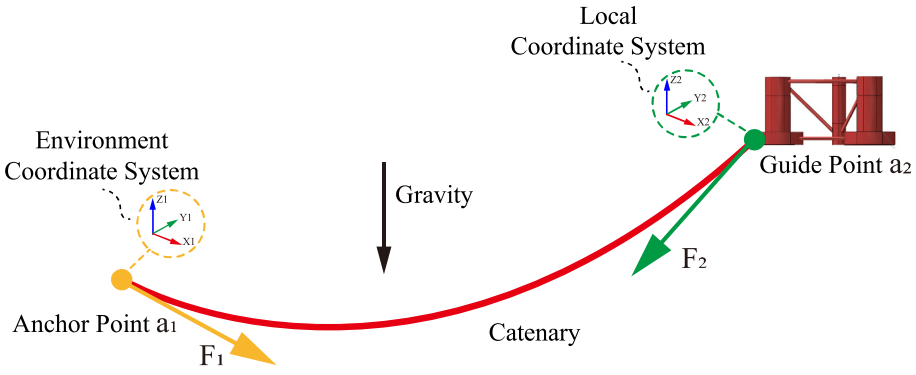

Fig. 4. Catenary forces in the DFBI model.

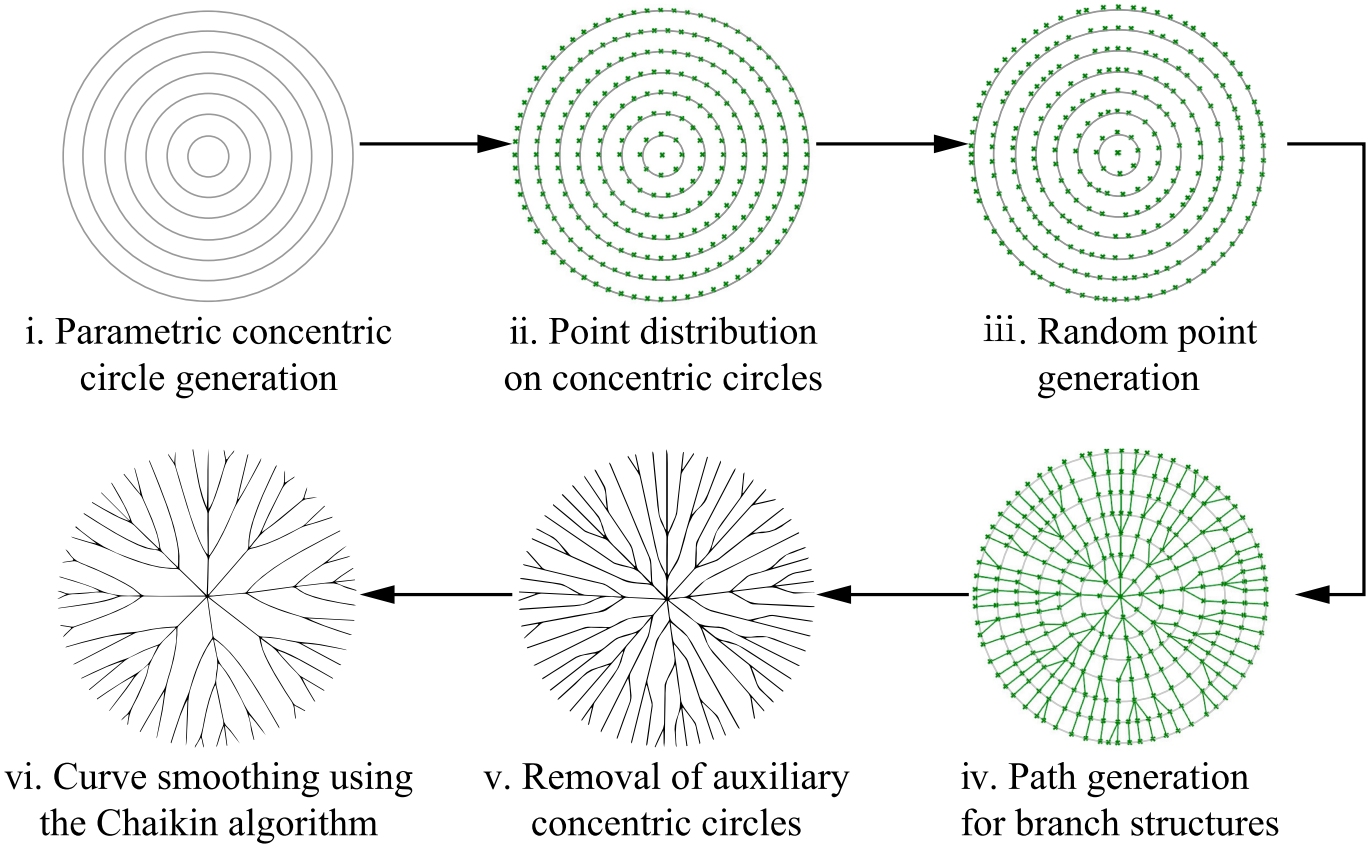

Fig. 5. Parametric modeling process of VA leaf venation branching.

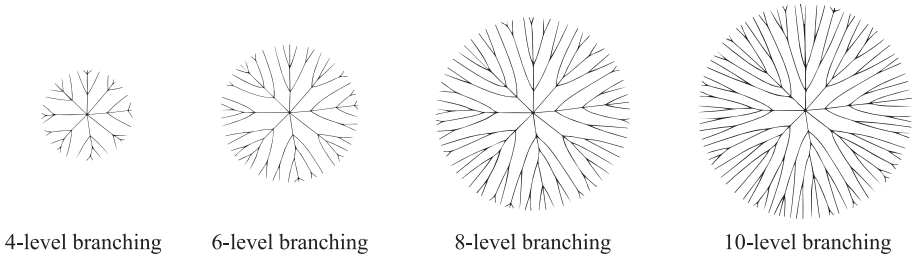

Fig. 6. Multi-level branching structure of VA.

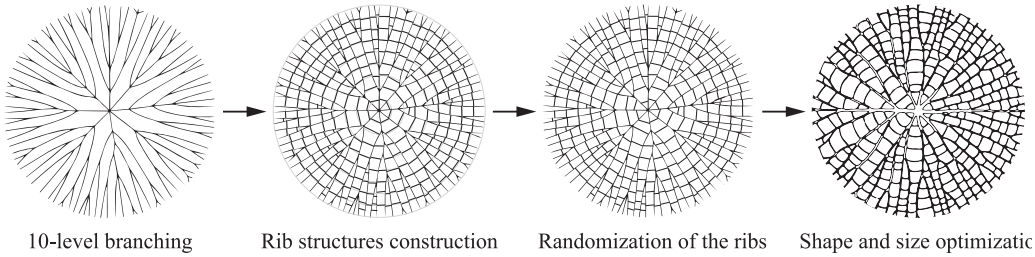

Fig. 7. Size and shape optimization of the VA parametric model.

3. Model description

3.1. Floating VAWT

This study focuses on a three-bladed H-type floating VAWT (see Fig. 8) mounted on the OC4 semi-submersible floating platform, with the geometric model referenced from Liu et al. [31]. The key difference in this study is that the blades, tower, and floating platform are modeled as rigid bodies, whereas in reference [31], the entire floating system was modeled as a shell to enable fluid-structure interaction (FSI) calculations, which are beyond the scope of this study. The primary geometric parameters of the floating VAWT are presented in Table 1, with more detailed modeling procedures available in [31].

In Fig. 8, the struts are generated by sweeping NACA airfoils with

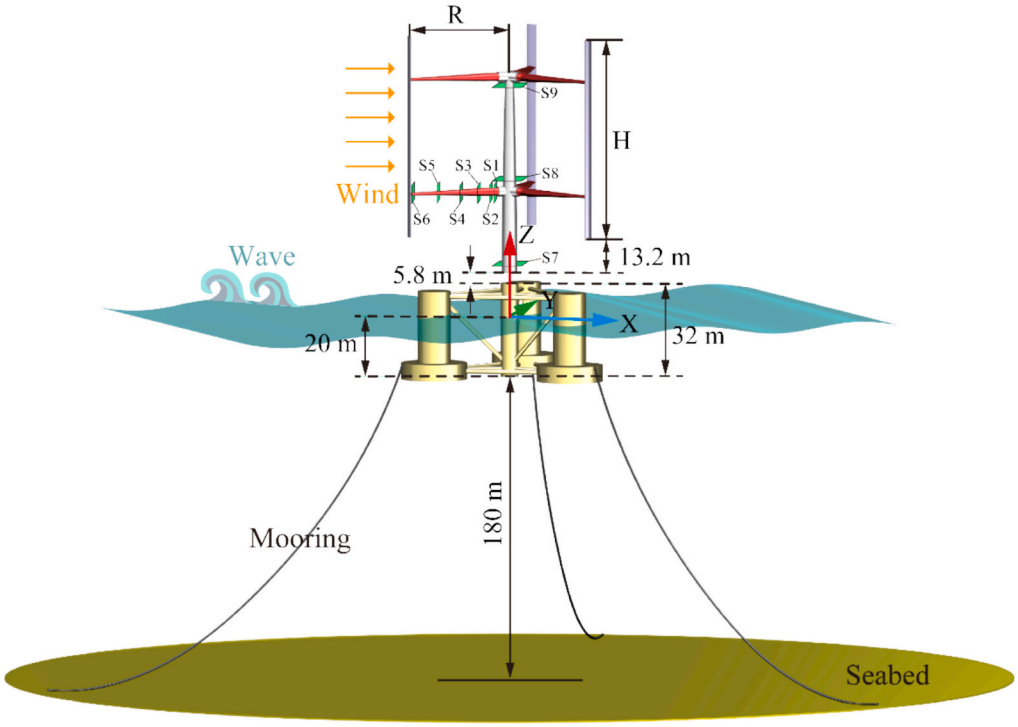

Fig. 8. Geometric model of the floating VAWT.

Table 1
Geometric parameters of the floating VAWT.

Parameter	Value
Blade Airfoil	DU-06-W-200
Number of Blades	3
Number of Support Rods per Blade	2
Blade Height H	70.25 m
Rotor Radius R	36.76 m
Blade Chord Length c	3.512 m
Blade Pitch Angle β	2°
Optimal Tip Speed Ratio λ	3.28
Rated Rotational Speed ω	6.81 rpm

varying thicknesses and chord lengths. The specific spatial positions (cross-sections S1 to S6) are shown in Fig. 9. The shaft is formed by sweeping circular cross-sections S7, S8, and S9, with corresponding diameters of 5.5 m, 5 m, and 3.5 m, respectively.

The OC4 semi-submersible platform [9], after modifications (which include changes to ballast water depth and platform component thickness), is used to support the proposed floating VAWT in this study. The platform was originally designed for the NREL 5 MW offshore HAWT [9], and its geometric model is shown in Fig. 10.

The platform's primary buoyancy is provided by the upper, lower, and main pontoons, which are interconnected by diagonal and cross braces. The upper and lower pontoons are arranged in a circular array along the Z-axis at 120° intervals, with internal ballast water to enhance the platform's resistance to tilting and overturning. The heights of the ballast water inside the upper and lower pontoons are 7.83 m and 5.17 m, respectively. Their main function is to maintain the platform's level and stability under varying wind and wave conditions. For ease of numerical modeling, adjustments were made to the connection points between the diagonal braces and the pontoons. In the original design, the diagonal braces were connected to the ends of the cross braces, as shown in light green in Fig.10a. The main parameters of the platform

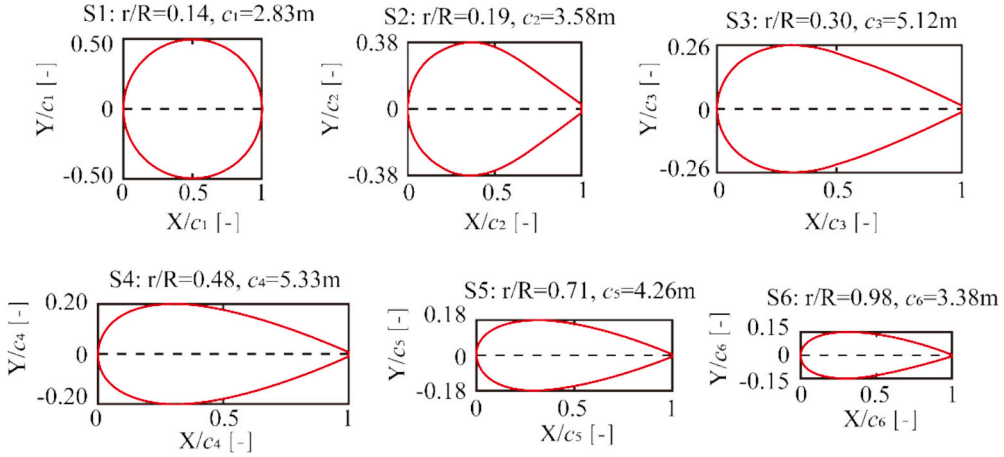

Fig. 9. Coordinates of different airfoil cross-sections for the struts.

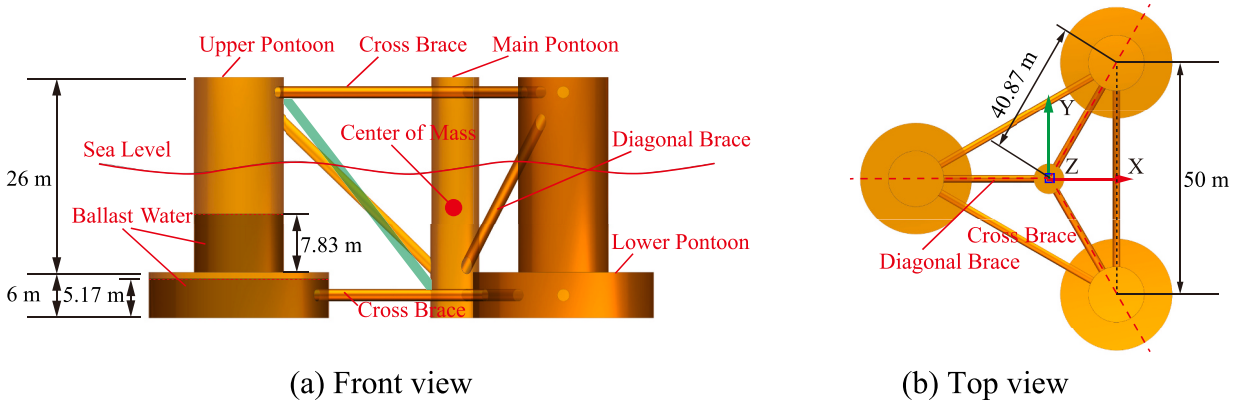

Fig. 10. Geometry model of semi-submersible platform.

related to mass are listed in Table 2, and additional geometric parameters can be found in [9].

To ensure platform stability, three catenaries (C1-C3) are connected to the platform at one end and anchored to the seabed at the other. C2 is aligned with the direction of the incoming wind and wave, while C1 and C3 are symmetrically arranged along the centerline of the incoming wind and wave. The three catenaries are arranged in a 120° circular array, as shown in Fig. 11.

It should be noted that the catenary modeling in DFBI for this study does not consider the interaction between the mooring lines and the seabed, which means that the entire system is in a suspended state. The mass-related parameters of the moorings are shown in Table 3.

3.2. Biomimetic platform

Based on the VA leaf venation parametric model in subsection 2.4, the model was imported into the CAD software NX 12.0 and extruded longitudinally (perpendicular to the plane) to form a three-dimensional (3D) solid. A subtraction operation was then performed between this solid and the lower pontoon of the semi-submersible platform. By adjusting the number of concentric circles, biomimetic structural configurations with varying vein levels were constructed, as shown in Fig. 12. For example, "3 levels" represents a VA structure established with three concentric circles in parametric curve.

In Fig. 12, VA leaf venations with 3 levels (VAS), 5 levels (VAM), and 7 levels (VAL) were selected to comparatively study the impact of different branch levels on the hydrodynamic performance of the semi-submersible platform. The VA leaf venation curves are extruded longitudinally to a height of 1 m, and the internal ballast water of the lower pontoon fills the entire cavity structure of the VA leaf venations. The material properties of the VA veins are consistent with those of the lower pontoon in the original platform. The established VA CAD model was imported into the finite element solver for modeling, and different material properties were assigned to the various components. The mass-related property parameters of the VA platform were then calculated, as shown in Table 4.

Table 2
Comparison of Mass-Related Properties of the Floating Platform with Literature.

Parameter	Value in Ref [9]	Value in FEM model	Error
Platform Mass (including ballast water)	1.3473×10^7 kg	1.3473×10^7 kg	0.0 %
Center of Mass (below waterline)	13.46 m	13.46 m	0.0 %
Roll Moment of Inertia I_{xx}	6.827×10^9 kg·m^2	6.56×10^9 kg·m^2	−3.9 %
Pitch Moment of Inertia I_{yy}	6.827×10^9 kg·m^2	6.56×10^9 kg·m^2	−3.9 %
Yaw Moment of Inertia I_{zz}	1.226×10^{10} kg·m^2	1.17×10^{10} kg·m^2	−4.6 %
Upper Pontoon Ballast Water Depth	7.83 m	7.83 m	0.0 %
Lower Pontoon Ballast Water Depth	5.0478 m	5.0478 m	0.0 %
Total Ballast Water Mass	9.6208×10^6 kg	9.6208×10^6 kg	0.0 %

As shown in Table 4, excluding ballast water, the mass of the VA platforms increases progressively with the venation levels: VAS, VAM, and VAL. This increase is due to the added material from the intricate leaf venation ribs, which expand the surface area at the bottom of the lower pontoon. For instance, the mass of the original platform increases from approximately 4.66 million kg to around 5.40 million kg in the VAL configuration. This additional material results in a downward shift of the center of mass relative to the waterline, from 7.42 m in the original platform to 9.25 m in the VAL platform. A lower center of mass improves stability by reducing the platform's tendency to tilt under wave action.

Moreover, the moments of inertia (I_{xx}, I_{yy}, and I_{zz}) for the VA platforms are higher than those of the original platform and increase with higher venation levels. For example, I_{zz}, which represents the resistance to yaw, increases from 3.32×10^9 kg·m^2 in the original platform to 4.02×10^9 kg·m^2 in the VAL configuration. This increase in inertia indicates that the VA platforms exhibit stronger resistance to rotational motions, such as roll, pitch, and yaw, thus enhancing the stability of the platform, particularly in turbulent wave conditions.

After considering ballast water, the mass-related property parameters of platforms with different VA leaf venation levels are shown in Table 5. The total mass of the VA platforms becomes similar to that of the original platform, despite the added structure material. This is because the VA structure reduces the internal volume of the lower pontoon, thus decreasing the amount of ballast water required to maintain buoyancy. For instance, while the original platform weighs approximately 13.27 million kg with ballast water, the VAL platform's total mass is comparable at around 13.25 million kg. This balance between increased structural mass and reduced ballast water volume keeps the platform's overall mass close to the original platform.

The center of mass (below the waterline) in Table 5 shows slight differences across configurations. For VAS and VAM, the center of mass shifts upward compared to the original platform due to reduced ballast water volume. However, the VAL platform retains a slightly lower center of mass (13.59 m) compared to the original, providing similar stability benefits as seen in Table 4. The moments of inertia (I_{xx}, I_{yy}, I_{zz}) in Table 5 are all higher than those in Table 4, illustrating that the inclusion of ballast water further increases the platform's resistance to rotational motion. For example, I_{zz} in the original platform rises from 3.32×10^9 kg·m^2 without ballast water to 1.11×10^{10} kg·m^2 with ballast. In the VA platforms, the moments of inertia also increase with ballast water. This increase in inertia provides even greater resistance to external wave forces, which is essential for maintaining the platform's stability under

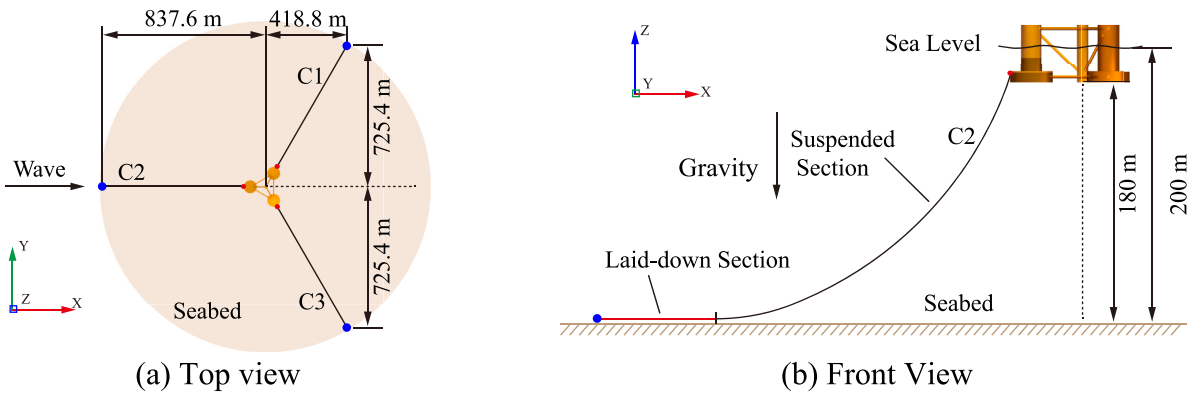

Fig. 11. Schematic Diagram of Catenary Arrangement.

Table 3
Mass-related parameters of mooring system.

Parameter	Value
Number of Mooring lines	3
Length in Relaxed State l_c	835.5 m
Catenary Diameter d_c	0.0766 m
Line Density	113.35 kg/m
Submerged Line Density	108.63 kg/m
Axial Stiffness	7.536×10^8 N/m

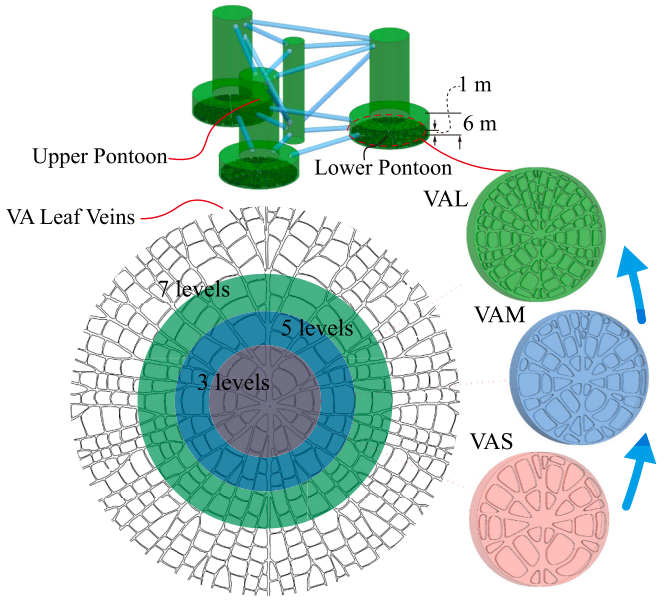

Fig. 12. Geometric models of the biomimetic Semi-Submersible platform with different VA leaf venation levels.

Table 4
Mass-related parameters of the VA platform (Excluding ballast water).

	Mass	Center of mass (below the waterline)	I_{xx}	I_{yy}	I_{zz}
Original	4,662,204.00 kg	7.42 m	2.24×10^9 kg·m^2	2.24×10^9 kg·m^2	3.32×10^9 kg·m^2
VAS	4,958,194.00 kg	8.34 m	2.43×10^9 kg·m^2	2.43×10^9 kg·m^2	3.61×10^9 kg·m^2
VAM	5,111,399.50 kg	8.67 m	2.52×10^9 kg·m^2	2.52×10^9 kg·m^2	3.75×10^9 kg·m^2
VAL	5,398,611.00 kg	9.25 m	2.68×10^9 kg·m^2	2.68×10^9 kg·m^2	4.02×10^9 kg·m^2

Table 5
Mass-related parameters of the VA platform (Including ballast water).

	Mass	Center of mass (below the waterline)	I_{xx}	I_{yy}	I_{zz}
Original	13,266,384.00 kg	13.54 m	6.42×10^9 kg·m^2	6.42×10^9 kg·m^2	1.11×10^{10} kg·m^2
VAS	12,961,543.00 kg	13.46 m	6.28×10^9 kg·m^2	6.28×10^9 kg·m^2	1.08×10^{10} kg·m^2
VAM	12,864,447.00 kg	13.42 m	6.23×10^9 kg·m^2	6.23×10^9 kg·m^2	1.08×10^{10} kg·m^2
VAL	13,248,885.00 kg	13.59 m	6.42×10^9 kg·m^2	6.42×10^9 kg·m^2	1.11×10^{10} kg·m^2

operational conditions.

4. Numerical modeling and verification

4.1. Computational domain and numerical setting

The 3D computational domain contains an upper air region and a lower water region. The air region is 1200 m in length, 500 m in width, and 300 m in height, while the water region extends to a depth of 200 m, as shown in Fig. 13. The floating VAWT is positioned 300 m from the velocity inlet, anchored to the seabed by three catenaries (C1-C3). It is noted that the seabed is not considered in the numerical model due to the fact that quasi-static method is used for catenary modeling. An overset strategy is applied in the VAWT and platform regions to allow for VAWT rotation and the platform's six degrees of freedom (six-DOF) motion. The grid is refined near the air-water interface and in the rotor wake region to better capture turbulence development. By varying the grid sizes in the VA structure region, three different grid configurations—VAS, VAM, and VAL—were developed to compare the effects of different VA leaf venation levels on the aero-hydrodynamic performance of the individual platform and the integral floating VAWT system.

The grid numbers for the individual platform and the floating VAWT with different VA leaf venation levels are shown in Table 6.

The Shear-Stress Transport (SST $k-\omega$) turbulence model [56], based

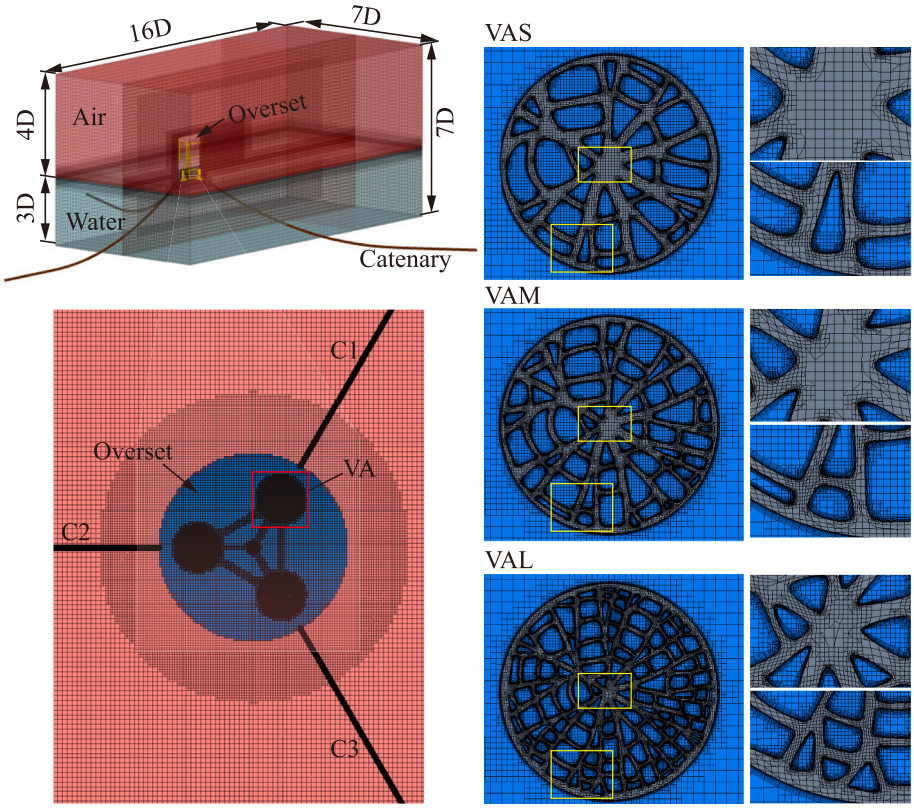

Fig. 13. Mesh distribution of the floating VAWT with different VA leaf venation levels.

Table 6
Grid number for the individual platform and floating VAWT.

Parameter	Original	VAS	VAM	VAL
Grid size in VA region	0.6 m	0.3 m	0.2 m	0.1 m
Grid number of Individual platform	7,883,350	9,227,961	9,864,777	10,545,307
Grid number of Floating VAWT	15,824,550	17,077,261	17,668,759	18,426,709

on the RANS method, has been proven to be suitable for evaluating the aerodynamic performance of VAWTs in terms of both computational efficiency and accuracy [57,58]. Since this paper does not focus on wind turbine airfoil optimization, tip design, or detailed local descriptions, but rather on the overall performance of the floating VAWT, the SST $k-\omega$ turbulence model was chosen for subsequent numerical simulations.

A time step sensitivity analysis was conducted using six different time steps (Δt), ranging from 0.05 s to 0.005 s. The impact of varying time steps on the torque of VAWT blade during one complete rotation after achieving stable rotation is shown in Fig. 14.

As seen in Fig. 14, the torque differences across different time steps are primarily observed at azimuth angles of 90° and 240°, with the most noticeable differences occurring around 90°. Outside this range, the curves nearly overlap. When the time step Δt decreases from 0.05 s to 0.04 s, the torque peak at 90° gradually increases, with minimal relative variation. Only when Δt reduces to 0.03 s do noticeable fluctuations appear in the peak torque value. As Δt further decreases, the changes become negligible, and a time step of Δt = 0.01 s is found sufficient to meet the accuracy requirements. This step size ensures that the rotation displacement per time step remains below half of a grid cell, facilitating data convergence.

The VOF wave model was employed to generate regular waves with a wave height of 7.58 m and a wave period of 12.1 s. These wave

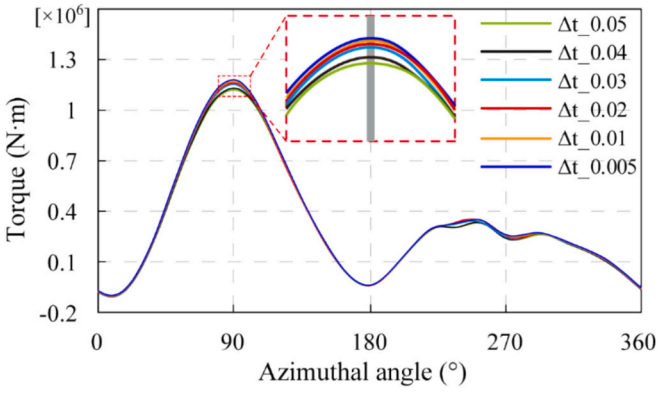

Fig. 14. Torque variation of VAWT blade with azimuthal angle under different time steps.

parameters are representative of extreme sea states commonly observed in high-wave regions of the North Atlantic Ocean. In particular, similar wave heights and periods have been recorded near the location 60.8°N, −27.8°W. This alignment with real-world conditions enhances the relevance of our study for assessing the performance of bio-inspired platform under severe ocean environments. To prevent wave reflection in the pressure outlet region, wave damping was applied within a 600 m range from the pressure outlet to ensure numerical stability and convergence.

4.2. Turbulence model validation

Battisti et al. [59]. conducted an experimental study at the high-speed wind tunnel of Politecnico di Milano (Fig. 15a), focusing on the performance comparison of H-type (Fig. 15b) and Φ-type VAWTs. Both

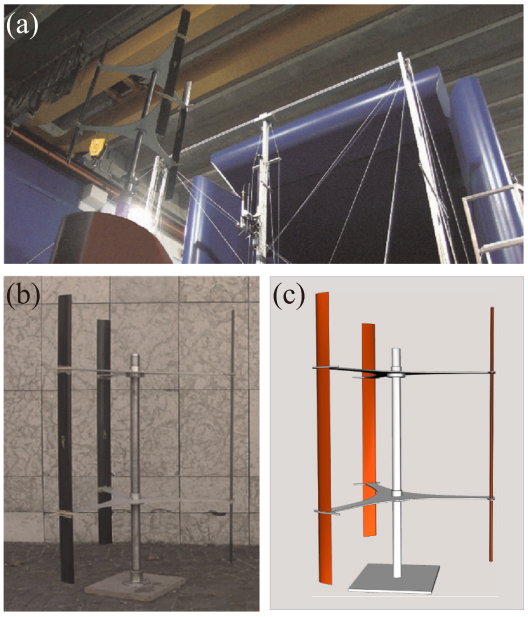

Fig. 15. Wind tunnel experiment of H-type VAWT.

turbines shared the same swept area and blade airfoil profile. The comprehensive data and geometric models obtained from this experimental work provide a solid foundation for validating numerical tools. Since the objective of this paper is a three-bladed H-type VAWT, only the H-type VAWT from the wind tunnel experiment is used for numerical simulation. Fig. 15c is the geometric model built in this paper, which is identical to the one used in Battisti et al.

Fig. 16 shows the 3D computational domain grid. At 1.5R and 3R (where R is the rotor radius) from the VAWT's center of rotation, 21 wake velocity monitoring points were set along the Y-direction at the midsection of the VAWT (marked by yellow solid lines). The spacing between each monitoring point is 0.1 m, used to monitor the wake velocity behind the rotor.

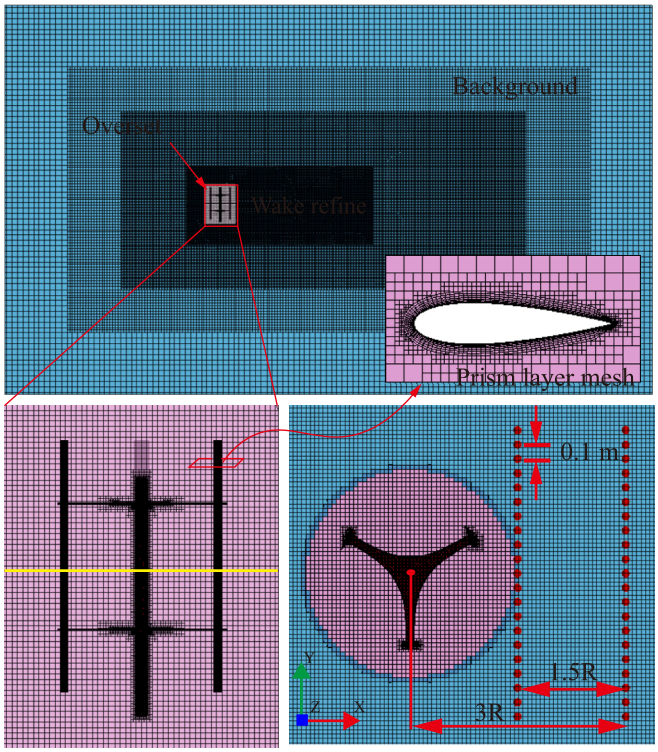

Fig. 16. Numerical model of wind tunnel experiment.

The entire computational domain was divided into orthogonal hexahedral structured grids, with mesh refinement in the wake region. The grid size in the refined region is 0.033 m, and the total number of grid cells reaches 8,531,827. The SST$k-\omega$ turbulence model was employed to simulate the boundary layer flow and wake development of the VAWT. A pressure-velocity coupling algorithm was used to address the coupling between the pressure and velocity fields, and the convective terms were discretized using a second-order upwind scheme to improve simulation accuracy. The time step was set to 2.08×10^{-4} s, corresponding to a rotor rotation of 0.5° per time step. The total simulation time was 3 s, covering approximately 20 full rotation cycles. The data from the final stable rotation cycle, averaged over two complete rotations, were used for comparison with experimental results.

Fig. 17 shows the variation of the power coefficient (C_p) with the tip speed ratio (TSR) for both the present CFD and experimental results, with the relative errors summarized in Table 7. It can be observed that for TSR below 3.30, the CFD results generally align with experimental data, particularly within the transition and dynamic stall regions. In these regimes, five data points fall within the experimental confidence interval, indicating acceptable agreement. At higher TSRs, however, the CFD model tends to overpredict the power coefficient due to increasingly influential secondary effects, such as complex turbulence patterns, blade-wake interactions, and vortex shedding dynamics. These effects challenge the capabilities of the RANS turbulence model, which struggles to fully capture the intricate, unsteady vortical structures and turbulent flows present at high TSRs.

Fig. 18 shows the distribution of wake velocity and turbulence intensity at the midsection of the VAWT at $x/R = 1.5$ and $x/R = 3$. Under different TSR conditions, the SST$k-\omega$ turbulence model was able to reproduce the experimental results well and demonstrated a high degree of consistency. In particular, in $\pm y/D > 0.5$ regions, the simulation results almost coincide with the experimental values, with the main deviations occurring near the wake centerline. This is due to the vortex shedding and mixing interactions between the VAWT blades, which the RANS turbulence model has difficulty capturing, especially when complex turbulence involves strong vortices and unsteady effects. Overall, considering the trade-off between accuracy and computational resource limitations, the SST model provides relatively reasonable results.

4.3. Free-decay performance

The free decay test is commonly used in wave basin to determine the natural period of floating systems. In 2011, the OC4 project conducted a free decay test of a 1/50 scale floating 5 MW HAWT mounted on a semi-submersible platform in the MARIN wave basin [60]. To simplify the

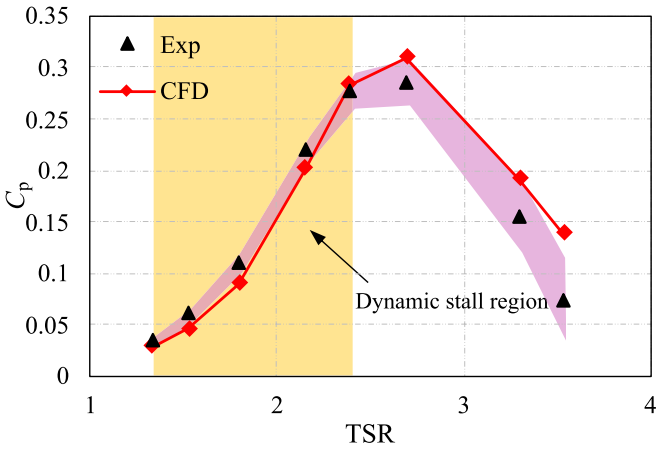

Fig. 17. Curve of power coefficient versus tip speed ratio.

Table 7
Comparison of Experimental and CFD Results with Relative Error.

TSR	C_p	Error %
1.33	0.02847	−14.17
1.51	0.04545	−24.30
1.80	0.08992	−18.35
2.16	0.20175	−8.37
2.40	0.28335	2.18
2.70	0.30996	8.62
3.30	0.19113	24.12
3.50	0.13844	88.30

computation, the HAWT blades and nacelle are simplified as an equivalent concentrated mass (ECM) acting at the top of the tower, as shown in Fig. 19. The initial surge displacement of the platform is set to 22 m, and the initial pitch angle is set to 8°.

Table 8 details the mass-related parameters of the floating system, which were calculated by the finite element solver (Abaqus 2022) and then used as inputs for the predefined parameters in DFBI continuum body. A comparison with the modeling parameters from Ref. [61] demonstrates the accuracy of the equivalent model established in this paper.

The time-varying surge and pitch free decay curves calculated in this study are shown in Fig. 20 and are compared with the DFBI results from Ref. [62] and the naoeFoam results from Ref. [63].

The results in both surge and pitch responses indicate that the present CFD results align closely with the DFBI model in Ref. [62], especially in terms of the overall decay behavior and amplitude. The naoeFoam model [63] shows slightly different results, particularly in terms of decay rates, but the general trend and behavior are still quite consistent. The comparison suggests that the present results provide a reliable prediction of the platform's hydrodynamics.

5. Results and discussion

This section analyses the impact of VA leaf venation with varying levels (VAS, VAM and VAL) on the hydrodynamic response of the individual platform, aiming to evaluate its potential to enhance stability and the underlying mechanisms involved. Subsequently, the VAL configuration will be applied to the integrated floating VAWT system to investigate the aero-hydro coupling performance, with the objective of further verifying its ability to reduce power output fluctuations.

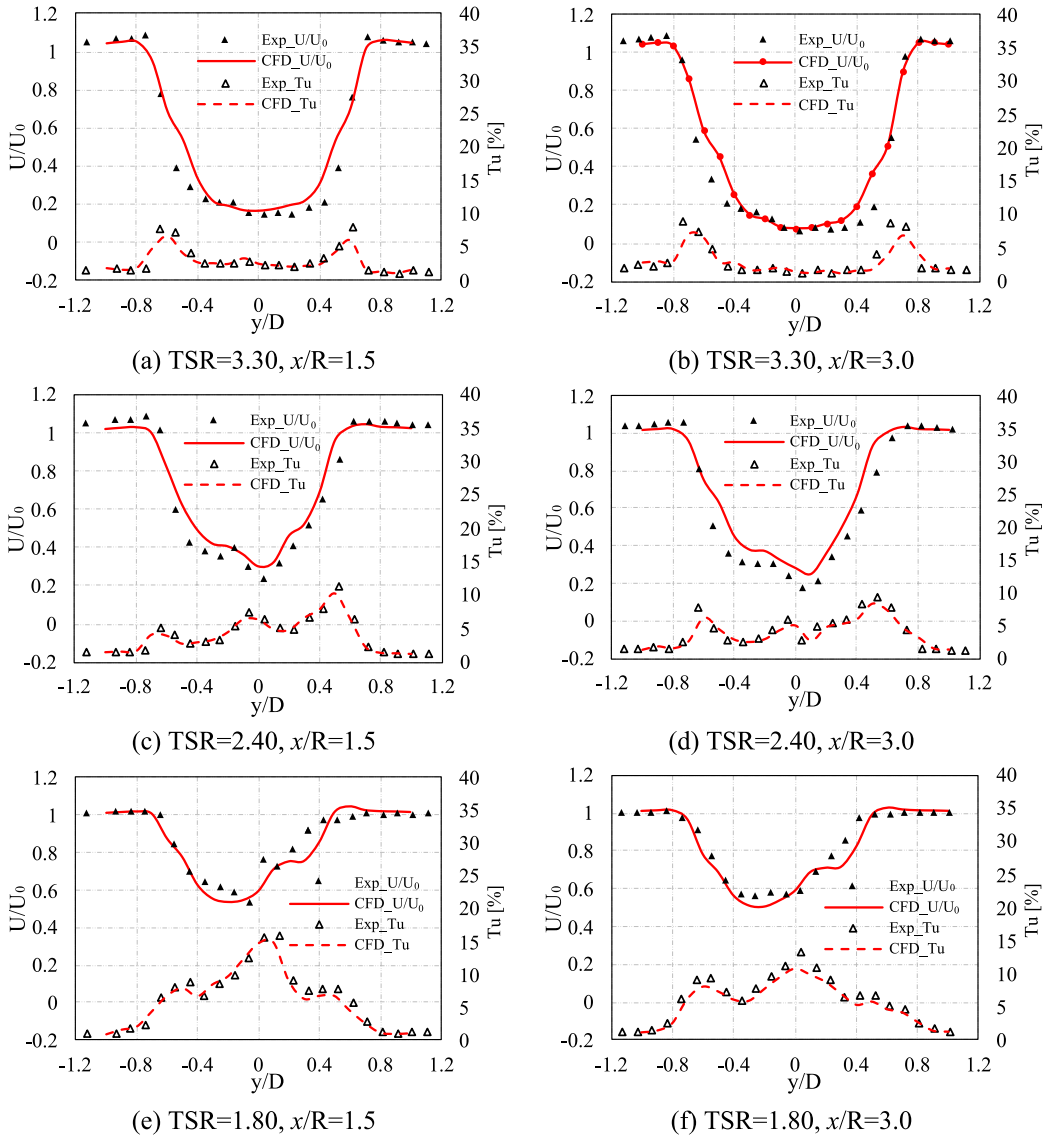

Fig. 18. Wake velocity at mid-section of VAWT for different TSRs.

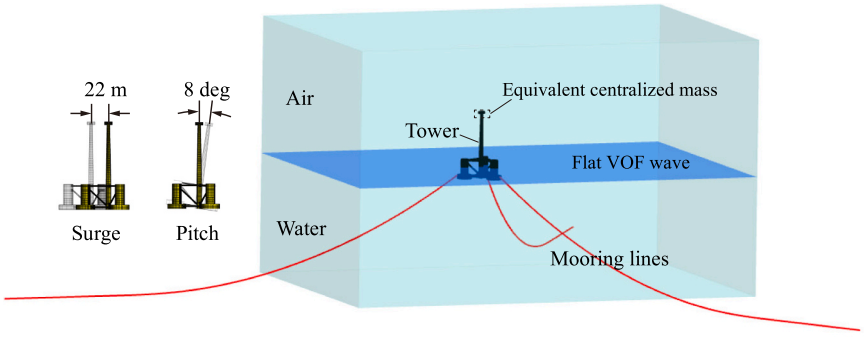

Fig. 19. Schematic diagram of free decay test for OC4 platform.

Table 8
The mass-related parameters of floating system.

	Mass	Difference	Center of Mass (below waterline)	Difference
Tower	249,718.03 kg	0.007 %	−44.3 m	2.1 %
Platform	13,473,097.00 kg	0.023 %	13.46 m	0.0 %
ECM	350,061.81 kg	0.018 %	−87.6 m	0.0 %
Total	14,072,876.00 kg	0.020 %	9.84 m	0.98 %

5.1. Impact of VA on the semi-submersible platform

In this subsection, the physical mechanisms by which the VA configurations enhance platform stability will be analyzed, focusing on the platform's six-DOF response, flow field, and mooring line tension. The results will lay the foundation for the subsequent analysis of the VA structure applied to floating VAWTs.

5.1.1. Six-DOF motion and rotational energy

The time-domain response curves of the rotational DOF (roll, pitch, and yaw) and translational DOF (surge, sway, and heave) for the original platform, as well as the floating platform with various VA configurations, are shown in Fig. 21.

In Figs. 21a-c, the roll and yaw responses of both the original platform and the platforms with different VA configurations gradually increase over time, but do not exhibit a distinct or consistent pattern. The roll response remains within [−0.02, 0.02] °, while the yaw response fluctuates between [−0.4, 0.4] °. Since both responses stay below 1°, this indicates that the VA structure has a very minimal impact on the roll and yaw motions of the platform.

After $t > 120$ s, the pitch response begins to exhibit a clear and regular pattern, although the amplitude varies among the platforms. Unlike the roll and yaw responses, the pitch response displays a much wider range, fluctuating between [−2,2] °. This increased sensitivity in the pitch motion is primarily attributed to the interaction between wave crests and troughs, as the wavelength significantly exceeds the platform's characteristic length. Consequently, the platform's rotational DOF in pitch becomes more sensitive than in other directions.

To further analyze the impact of different VA-inspired designs on the pitch response of the floating platform, the time interval between 330 and 360 s, which contains two complete wave periods, was selected, as shown in Fig. 22.

It can be observed that all VA configurations effectively reduce the platform's pitch response, with higher leaf venation levels providing better suppression. The pitch fluctuation amplitude of the original platform is 3.268°. Among the three VA designs, the VAL configuration shows the greatest improvement, reducing the pitch amplitude to 2.318°, a 38 % decrease compared to the original platform. The VAM configuration follows, while the VAS has the least effect, reducing the pitch amplitude to 2.834°, representing a 16 % reduction.

Figs. 21 d-f show the impact of VA designs on the translational DOF (surge, sway, and heave) of the floating platform. For surge, the response curves of the original platform and those incorporating VA structures are nearly identical, with only a slight difference in peak amplitude. For the most part, the curves overlap, indicating that the VA structure does not significantly affect the surge response. This is because the surge response is predominantly influenced by factors such as the wave incidence angle, wavelength, and platform geometry, and the VA structure does not substantially alter the contact area between the platform and incoming waves.

Between 240 and 360 s, the sway response of the platforms with different VA-inspired designs shows a noticeable increase compared to the original platform. This is due to the asymmetry introduced by the VA structures, which feature irregular chambers that cause uneven water contact on the lower pontoon of the platform relative to the wave-facing direction. However, the sway amplitude remains within a narrow range of [−1,1] °, indicating that the overall impact of the VA structure on sway response is negligible.

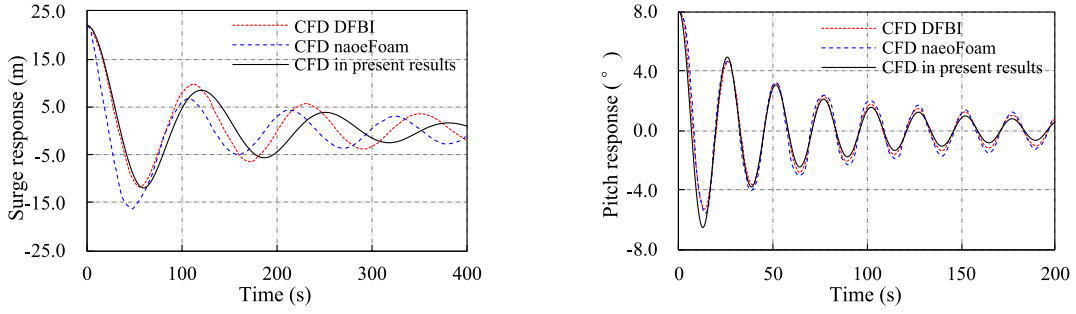

Fig. 20. The decay simulations of OC4 platform.

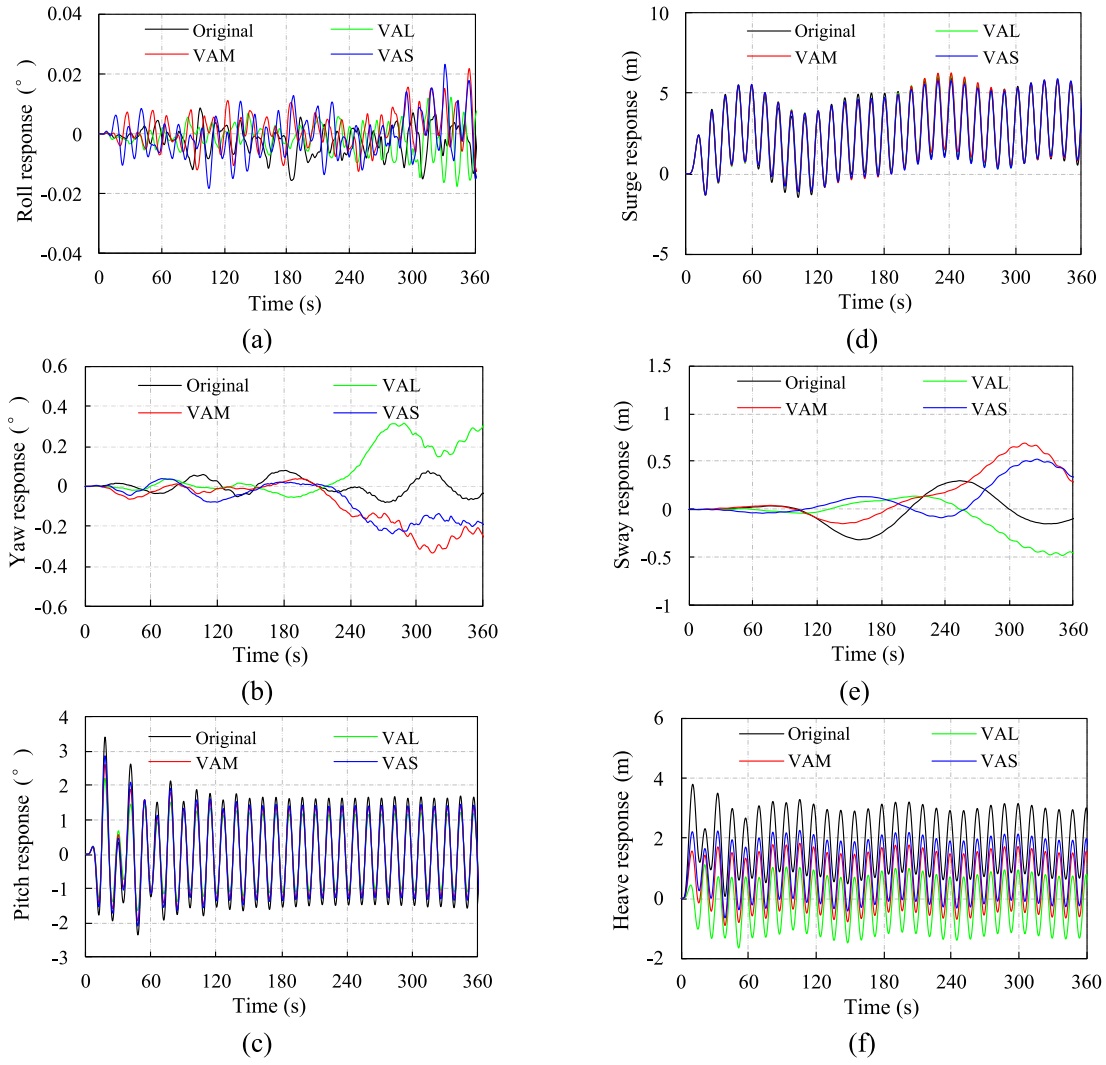

Fig. 21. Six-DOF response of the original platform and platforms with different VA leaf venation levels: (a)-(c), rotational DOF; (d)-(f), translational DOF;

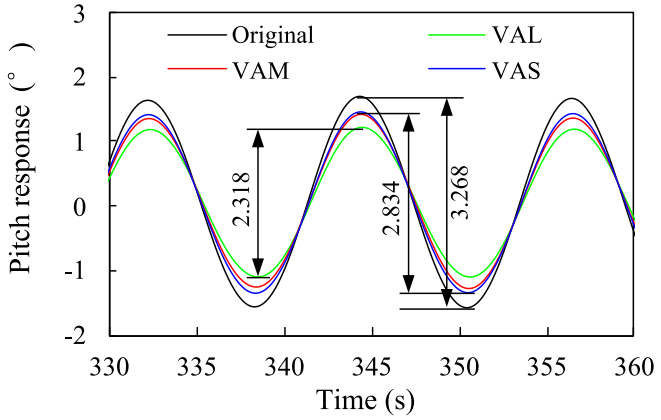

Fig. 22. Enlarged view of pitch response of different platform.

For the heave response, the average draft of the original platform increases by 1.16 m relative to the waterline due to the platform's reduced weight after excluding the VAWT. Platforms with different VA configurations exhibited a reduction in draft, with draft increasing progressively as the VA level rose. The average drafts for the VAL, VAM, and VAS were − 0.315 m, 0.425 m, and 0.82 m, respectively, relative to the waterline, representing reductions of 1.475 m, 0.735 m, and 0.34 m compared to the original platform. This is mainly because the VA structure reduces the displaced water volume, thereby lowering buoyancy and increasing draft depth.

To quantitatively analyze the impact of the VA structures on the platform's surge and heave responses, statistical values of surge and heave were calculated over the last two stable wave periods for both the original platform and the platforms with different VA configurations, as shown in Table 9 and Fig. 23.

From Table 9 and Fig. 23: (i) The maximum and minimum surge responses of the platforms with different VA configurations are higher than those of the original platform. This is because the VA structure

Table 9
Statistical values of surge and heave responses for the original platform and platforms with different VA leaf venation levels.

	Statistical values	Original	VAL	VAM	VAS
Surge	Maximum value	5.77 m	5.88 m	5.81 m	5.93 m
	Minimum value	0.80 m	1.08 m	0.97 m	1.05 m
	Fluctuation amplitude	4.97 m	4.79 m	4.84 m	4.87 m
	Standard deviation	1.83 m	1.76 m	1.78 m	1.79 m
Heave	Maximum value	2.95 m	0.73 m	1.51 m	1.93 m
	Minimum value	0.64 m	−1.36 m	−0.66 m	−0.29 m
	Fluctuation amplitude	2.32 m	2.09 m	2.17 m	2.22 m
	Standard deviation	0.80 m	0.73 m	0.75 m	0.77 m

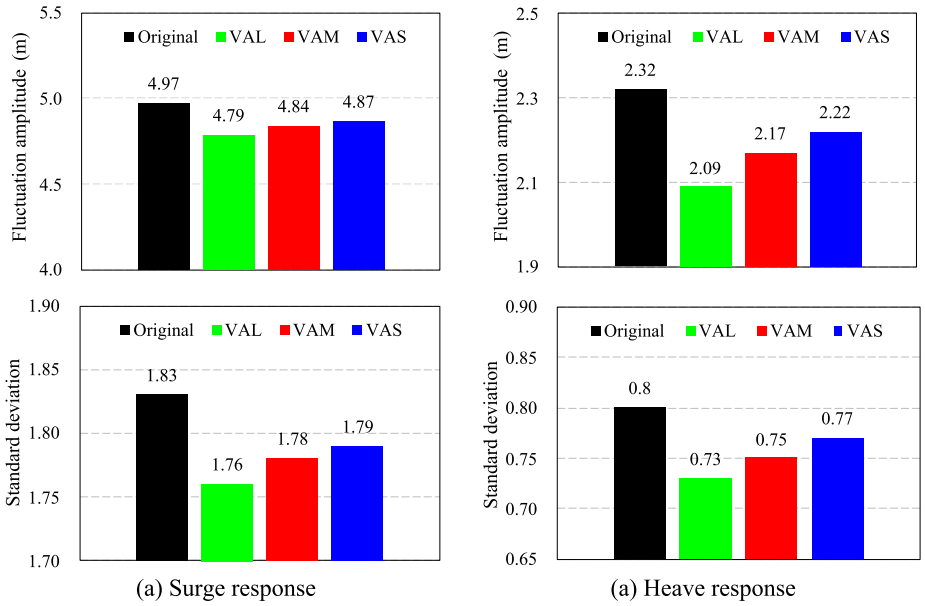

Fig. 23. Surge and heave amplitude and standard deviation for the original platform and platforms with different VA leaf venation levels.

increases the total contact area between the platform and the water, resulting in a greater overall wave force, which shifts the average equilibrium position of the surge response rearward. (ii) The fluctuation amplitude and standard deviation of the surge response for the VA platforms are lower than those of the original platform, with values approaching those of the original platform as the VA levels decrease. Compared to the original platform, the VAL, VAM, and VAS configurations reduce fluctuation amplitude by 3.6 %, 2.6 %, and 2.0 %, respectively, and reduce the standard deviation by 3.8 %, 2.7 %, and 2.2 %. This indicates that the proposed VA structure provides better surge stability than the original platform. (iii) The effect of the VA structure on the heave response follows a similar trend to surge response. The fluctuation amplitude and standard deviation of the heave response are both reduced compared to the original platform, with the impact diminishing as the VA levels decrease. Specifically, the VAL, VAM, and VAS configurations reduce the heave fluctuation amplitude by 9.9 %, 6.5 %, and 4.3 %, respectively, and reduce the standard deviation by 8.8 %, 6.3 %, and 3.8 %, indicating that the VA platforms also exhibit better heave stability than the original platform.

Fig. 24 shows the time-varying curves of rotational energy for the original platform and the different VA platforms, along with a zoomed-in view of the final stable operating state.

As shown in Fig. 5.15, the rotational energy of different platforms fluctuates periodically within the range of 0–8 $\times$ 10^5 J after $t > 120$ s, due to the continuous influence of periodic external wave forces. The

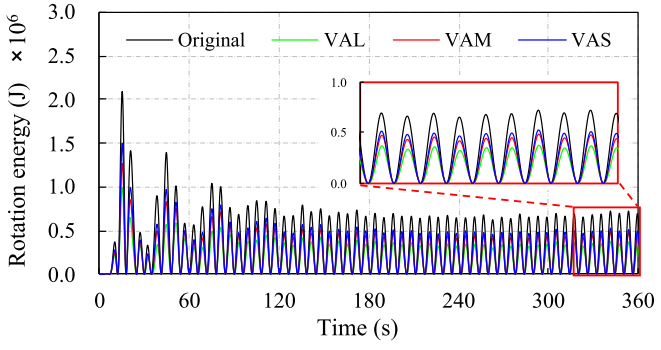

Fig. 24. Time history of rotational energy for the original platform and platforms with different VA levels.

different VA leaf venation levels effectively reduce the system's rotational energy. The maximum rotational energy for the VAL, VAM, and VAS configurations (4.09 $\times$ 10^5 J, 5.21 $\times$ 10^5 and 5.63 $\times$ 10^5 J, respectively) is reduced by 48 %, 34 %, and 29 % compared to the original platform (7.89 $\times$ 10^5 J). This indicates that the VA structure reduces the platform's response to external wave load disturbances, helping to maintain the stability of the platform. Additionally, lower rotational energy can reduce structural stress and fatigue caused by rotation, thereby extending the platform's service life.

5.1.2. *Flow field of the biomimetic platform*

To further investigate the physical mechanisms by which the VA structure enhances the stability of the floating platform, Fig. 25 shows the vorticity field contours at the bottom of the lower pontoon (Z = −19.5 m) for the original platform and VA-augmented platforms with different leaf venation levels. Fig. 25(a) illustrates the vorticity distribution during the platform's surge motion in the negative X-direction, while Fig. 25(b) presents the results for surge motion in the positive X-direction.

As shown in Fig. 25a, when the platform surges in the negative X-direction (opposite to the wind and wave direction), the velocity of the original platform relative to the waves is high. The waves directly impact the left pontoon, forming a significant vortex shedding region with a triangular pattern. The detached vortices extend from the left pontoon to the central pontoon, while the two pontoons on the right are situated in a low-energy turbulent zone behind the left pontoon's wake, resulting in minimal vortex formation.

For platforms with various VA structures, the intricate leaf venation design introduces numerous small-scale internal cavities, promoting more small-scale vortices across the platform surface. Unlike the original platform, the vortex distribution around the left pontoon in VA platforms is more widespread, extending not only behind the left pontoon but also to the central and right pontoons, resulting in a more uniform vortex field. As the venation level increases, the interaction between the internal cavities and the external fluid intensifies. This interaction effectively dissipates the kinetic energy of the platform and increases drag. Monitoring the platform's center-of-mass velocity reveals that the VA structure reduces the platform's motion speed. Compared to the original platform (−1.33 m/s), the velocities for the VAL, VAM, and VAS platforms decrease by 12.8 %, 8.3 %, and 3.8 %, respectively (−1.16 m/s, −1.22 m/s, and − 1.28 m/s). The specific physical mechanisms are as

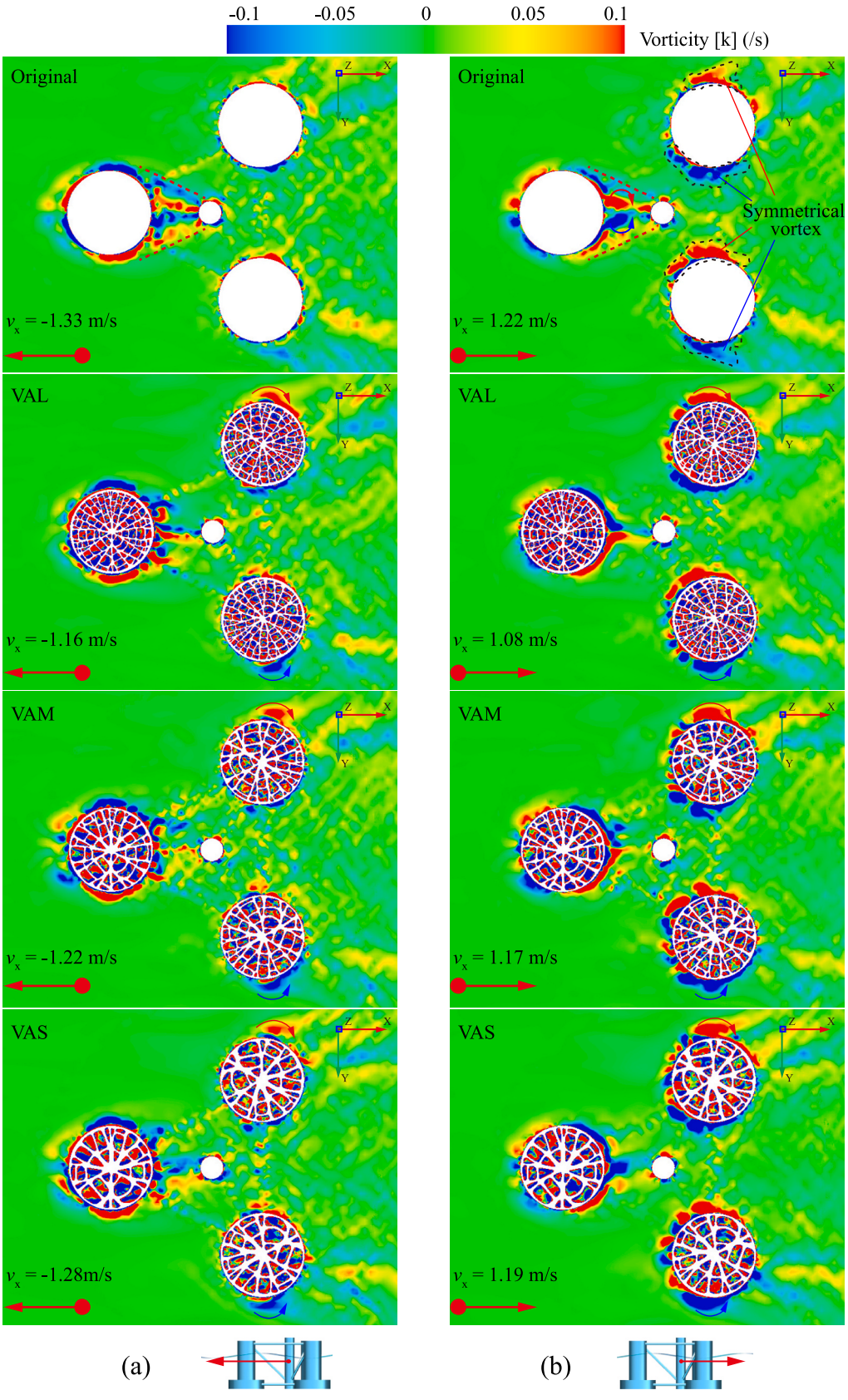

Fig. 25. Vorticity field contour at the bottom of the lower pontoon for the original platform and platforms with different VA leaf venation levels: (a) The direction of platform surge motion is along the negative X-direction, (b) the direction of platform surge motion is along the positive X-direction.

follows: i. The cavity design in the VA platforms enhances shear force and centrifugal force of fluid within the internal chambers, facilitating vortex formation. These vortices interact with the chamber walls, effectively dissipating wave energy, converting it to heat, and enhancing damping. ii. The VA structure's cavities increase the contact area between the fluid and the wall surfaces, thereby amplifying viscous effects. Viscosity is a primary driver of vortex generation, and the increased wall interactions significantly enhance vortex density, leading to effective absorption of wave energy. Iii. Higher venation levels (such as the VAL design) lead to a more uniform vortex distribution, allowing wave energy to dissipate more evenly across the platform's base. This reduces the instability associated with concentrated vortices around individual pontoons, further enhancing platform stability.

In Fig. 25b, when the platform surges in the positive X-direction (aligned with the wind and wave direction), the platform and waves travel in the same direction, resulting in a lower relative velocity between them. The wake of the left pontoon has a reduced shielding effect on the right pontoons, allowing waves with sufficient energy to reach the right pontoon, leading to new flow separation and vortex shedding. This configuration results in symmetrical vortex regions behind the left and right pontoons in the original platform. In contrast, the vortex distribution in the VA bio-inspired platform exhibits clear asymmetry. The random nature of the VA structure, with internal chambers of varying sizes, leads to differences in flow resistance and vortex strength as fluid passes through different chambers on the platform's base. This results in an asymmetric vortex pattern. These asymmetrical vortex regions create non-uniform moments on the platform, explaining the increase in yaw and roll responses observed in the VA platform (as noted in Fig. 21) compared to the original platform. Monitoring the center-of-mass velocity shows that, relative to the original platform (1.22 m/s), the VA platforms achieve a reduction of 11.5 % (1.08 m/s for VAL), 4.1 % (1.17 m/s for VAM), and 2.5 % (1.19 m/s for VAS).

In summary, the VA bio-inspired platform utilizes the cavity structure of the venation design to enhance wall viscous effects, which facilitates vortex generation. These vortices interact extensively with the chamber walls, effectively dissipating and absorbing wave energy, ultimately improving platform stability.

5.1.3. *Mooring lines tension*

The three catenaries (C1, C2, and C3) connected to the lower pontoons of the semi-submersible platform provide restoring moments during the platform's six-DOF motion, helping to maintain the dynamic equilibrium of the entire floating system. The time-varying tension curves of the mooring lines for both the original platform and the VA platforms are shown in Fig. 26.

As shown in Fig. 26, the tension in mooring line C2 is consistently higher than in mooring lines C1 and C3 because it is positioned on the wave-facing side, directly encountering wave forces, leading to greater horizontal loads and platform displacement. In contrast, C1 and C3, on the opposite side, experience lower tension as they primarily counteract the platform's motion, rather than resisting direct wave forces. Comparing the different platforms, the VA platform shows consistently lower tensions in C1 and C3 compared to the original platform, with greater reductions as the VA levels increase. Conversely, the tension in C2 is higher for the VA platform. This is due to the VA structure shifting the platform's average surge equilibrium position backward, increasing the slack in C1 and C3, thereby reducing their tension, while C2 experiences stronger pull from wave action, resulting in higher tension. The statistical values and safety factors for the mooring line tensions of the different platforms are shown in Table 10.

As shown in Table 10, the VA structure effectively enhances the safety factors for mooring lines C1 and C3, though it slightly reduces the safety factor for C2. According to the API-RP-2SK standard [64], since the mooring system in this study is calculated using a quasi-static method and the mooring system is assumed to be intact, the allowable mooring line tension is set at 50 % of the breaking strength,

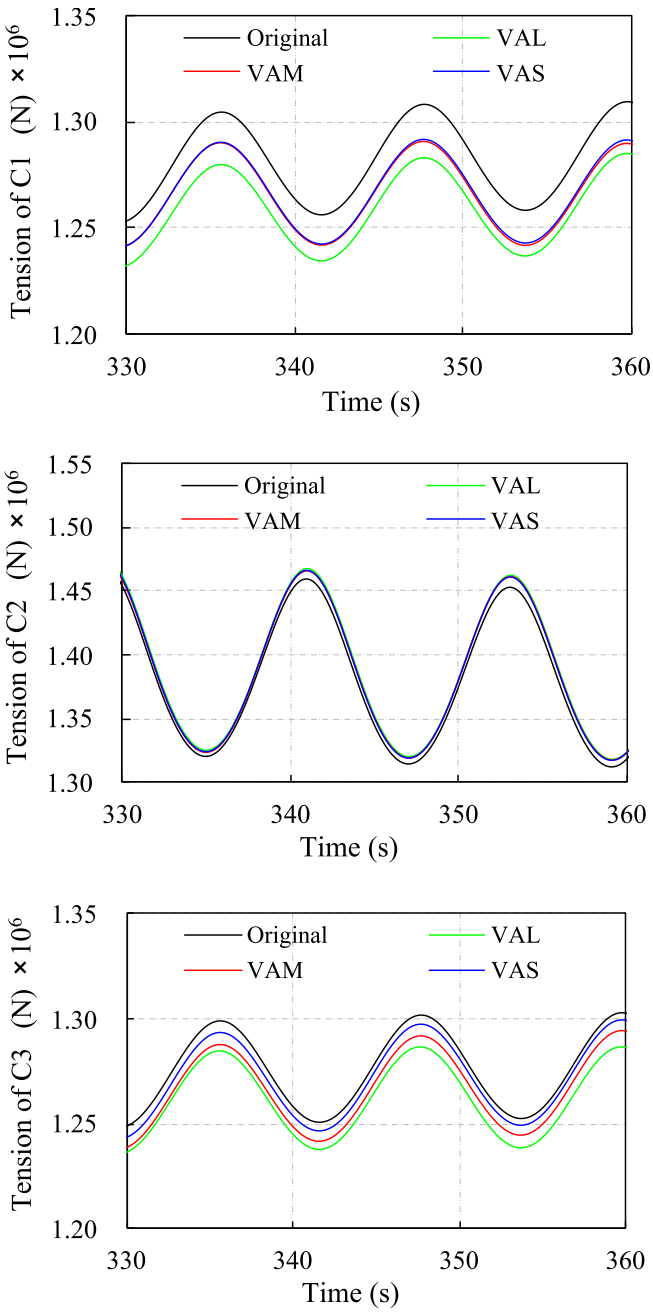

Fig. 26. Moorling lines tension of original platform and platforms with different VA levels.

Table 10
Safety factor analysis of mooring system.

	Catenary No.	Maximum	Minimum	Average	Safety Factor
Original	C1	1,309,587	1,252,616	1,280,663	5.73
	C2	1,469,464	1,311,957	1,383,297	5.10
	C3	1,302,946	1,248,172	1,275,106	5.76
VAL	C1	1,285,230	1,231,626	1,258,060	5.84
	C2	1,476,236	1,317,894	1,390,087	5.08
	C3	1,286,681	1,235,717	1,260,970	5.83
VAM	C1	1,290,870	1,240,583	1,265,341	5.81
	C2	1,473,324	1,317,342	1,388,507	5.09
	C3	1,294,443	1,237,986	1,265,793	5.79
VAS	C1	1,291,839	1,241,016	1,266,025	5.81
	C2	1,475,251	1,317,108	1,389,052	5.08
	C3	1,299,542	1,242,772	1,270,718	5.77

corresponding to a safety factor of 2.0. All the mooring safety factors in the table exceed 5.0, indicating that the VA platform's mooring system has substantial safety margins, ensuring the stability and security of the floating system.

5.2. Impact of VA on the floating VAWT

In this subsection, the VA structure is applied to the floating VAWT to assess its effectiveness. Only the VAL structure is considered, with its mass-related parameters detailed in Table 11. The VAL structure reduces the overall weight of the floating VAWT system, and the center of mass shifts downward by approximately 0.47 % relative to the waterline. The moment of inertia in different directions remains largely unchanged.

5.2.1. Power coefficient and flow field

Fig. 27 presents the time-varying power coefficient curves for the original floating VAWT and the floating VAWT with the VAL structure. The motion of the floating platform causes significant fluctuations and irregularities in the power coefficient curves, with values occasionally exceeding the Betz limit (59.3 %, the theoretical maximum for a stationary rotor in steady flow). This effect is primarily due to the platform's six degrees of freedom (DOF) motion, which alters the inflow conditions for the blades. When the relative velocity of the blades combines with the incoming flow, it can momentarily enhance the VAWT's energy capture efficiency.

By averaging the power coefficient over the last 10 stable revolutions of the floating VAWT, the power coefficient for the VAWT with the VAL structure is found to be 0.338, a decrease of approximately 0.86 % compared to the original VAWT (0.341). However, the VAL structure effectively reduces the fluctuation amplitude of the power coefficient curve, with a 10 % decrease in the standard deviation. This suggests that while the VAL structure has a limited impact on increasing the average power coefficient, it significantly improves the overall stability of power output.

Fig. 28 shows the velocity and vorticity field contours for the floating VAWT, with the airflow region displaying the velocity field and the water region showing the vorticity field.

As shown in Fig. 28, under the influence of wind and wave loads, a velocity deficit forms directly behind the floating VAWT, with unstable wake dissipation observed near the blade tips and tower. For the original floating VAWT, a recirculation zone appears behind the platform, while the VAL platform exhibits a smaller recirculation zone in the same area due to its increased draft depth. Comparing the vorticity field distribution along the Y-direction around the platforms, it is clear that the internal cavity structure of the VAL platform captures more vortices, creating a more complex interaction with the surrounding fluid. This results in large areas of opposing vortices at the platform's bottom. The increased number of vortices leads to greater energy dissipation, altering the fluid flow pattern and reducing the platform's dynamic response. In contrast, the original platform, with its smooth and flat bottom structure, generates smaller vortex areas around the platform.

5.2.2. Six-DOF motion and rotational energy

The time-varying six-DOF response curves for the floating VAWTs with and without the VAL structure are shown in Fig. 29.

Similar to the analysis of the individual platform in Subsection 5.1, the surge, pitch, and heave responses of the floating VAWT are significantly larger than the other three DOF (roll, sway, and yaw). This is mainly due to the following reasons: (i) The rising and falling of waves directly affect the platform's heave motion. (ii) The wave incidence direction aligns with the surge direction, leading to greater horizontal displacement. (iii) The wavelength of the regular waves is much longer than the platform's characteristic length, resulting in a pronounced pitch response. Table 12 presents the statistical values and standard deviations for the surge, pitch, and heave responses of both the original floating VAWT and the floating VAWT with the VAL structure.

It can be observed that: (i) For the surge response, unlike the individual platform, the VA structure does not shift the overall equilibrium position backward as significantly for the entire floating VAWT system. Instead, the fluctuation range [4.35, 8.94] m is smaller than that of the original floating VAWT [3.79, 9.04] m, with a 4.3 % reduction in standard deviation. This indicates that the VAL structure further improves the surge response when applied to the entire floating VAWT system. (ii) For the pitch response, the maximum value for the original floating VAWT is 2.43, while it is reduced to 2.03 for the VAL floating VAWT, decreasing the overall fluctuation amplitude by 12.4 % and the standard deviation by 22.8 %. This effectively reduces the platform's pitching motion and explains the improved stability of the VAWT's power coefficient. (iii) For the heave response, the internal cavity structure of the VAL reduces the platform's displacement area, resulting in about a 2 m decrease in draft compared to the original platform. However, the overall fluctuation amplitude and standard deviation are reduced by 8.1 % and 8.8 %, respectively, indicating that the floating VAWT with the VA structure exhibits better heave stability.

The time-varying curve of rotation energy for the floating VAWT throughout the entire operation is shown in Fig. 30.

As shown in Fig. 30, the VAL structure effectively reduces the rotational energy of the floating system. At $t = 346$ s, the peak rotational energy is reduced by up to 32 %, indicating that the VAL structure helps absorb or dampen the rotational kinetic energy induced by wind and wave loads, thereby improving the overall stability of the system. This effect is particularly beneficial for large-scale VAWTs, as it can reduce structural stress and blade aero-elastic responses caused by rotation, ultimately extending the lifespan of the structure.

5.2.3. Coupled aero-hydro analysis

To further analyze the impact mechanism of the VAL structure on VAWT blade torque, the torque fluctuations of the blades are examined in relation to the platform motion, as shown in Fig. 31. Figs. 31b and c depict the surge and pitch responses of the floating VAWT over two complete wave periods, while Fig. 31a shows the torque of Blade 1 (B1) over the same time range. The focus is on the surge and pitch responses, as these responses more directly alter the inflow conditions for the VAWT blades.

As shown in Fig. 31a, the torque curve for Blade 1 (B1) of both the original floating VAWT and the floating VAWT with the VAL structure exhibits periodic fluctuations within each rotation. In the range [0, T1/3], the blade is on the windward side, and as the angle of attack increases, the thrust on the blade grows, reaching a peak torque at T1/4. Afterward, the angle of attack decreases, leading to reduced thrust in the range [T1/4, T1/3], with the torque reaching a minimum at T1/2. On the leeward side [T1/2, T1], B1 is affected by the wake of the upstream blades, causing the actual inflow wind speed to decrease, resulting in a flatter torque curve during this phase.

The primary difference in blade torque between the floating VAWTs with and without the VAL biomimetic structure lies in the torque peak.

Table 11
Mass-related parameters of floating VAWT with VAL structure.

	Mass	Center of mass (below the waterline)	I_{xx}	I_{yy}	I_{zz}
Original	14,767,593.00 kg	−6.41 m	1.39e+10 kg·m^2	1.39e+10 kg·m^2	1.14e+10 kg·m^2
VAL	14,750,094.00 kg	−6.44 m	1.39e+10 kg·m^2	1.39e+10 kg·m^2	1.14e+10 kg·m^2

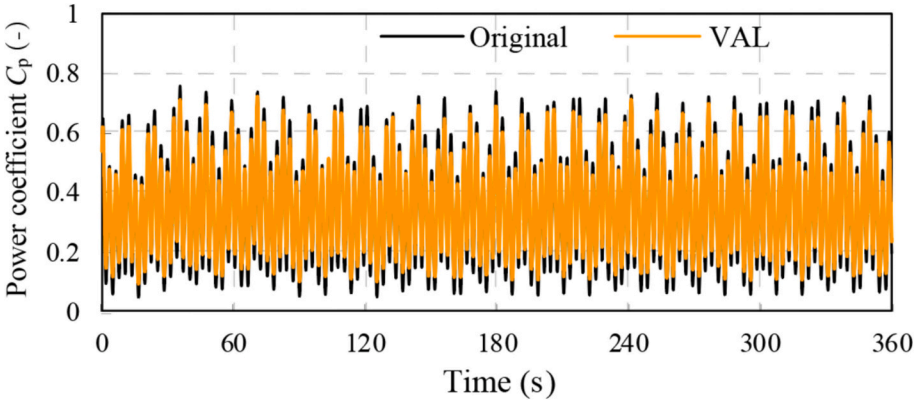

Fig. 27. Comparsion of power coefficients for floating VAWT with and without VA configuration.

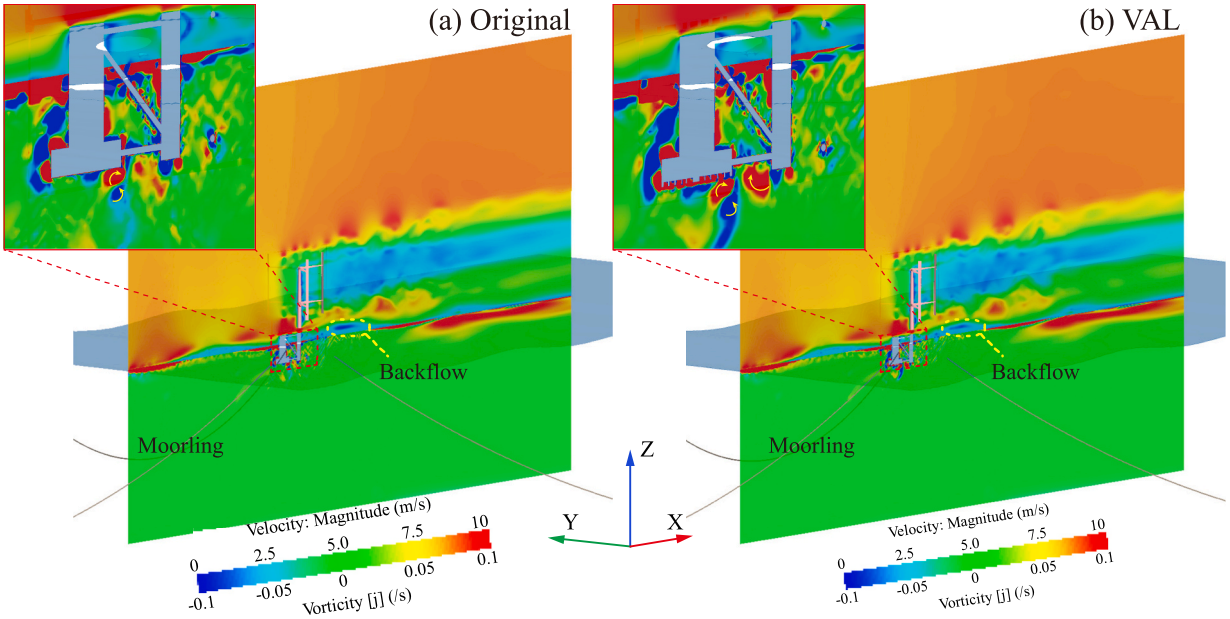

Fig. 28. Comparsion of velocity and vorticity contours for floating VAWT with and without VA configuration.

In the [0, T1/3] range, the platform undergoes surge motion in the negative X-direction (Fig. 31b), causing the blade's relative velocity to combine with the incoming wind speed, enhancing the torque. However, as seen in Fig. 31c, the platform also experiences a positive pitch motion, and the pitch angle of the original floating VAWT is larger than that of the VAWT with the VAL structure. This greater pitch in the original platform results in more forward movement of the blades in the positive X-direction, reducing the wind-speed overlap effect. Consequently, the torque peak for the VAL-configured floating VAWT is significantly higher than that of the original platform in this range.

In the [T1, 4 T1/3] range, the platform's surge response is at its equilibrium position, and the pitch angle is close to 0°. During this period, the platform's dynamic response has little effect on the blade's inflow angle, resulting in minimal torque peak differences between the floating VAWTs with and without the VAL structure.

In the [2 T1, 7 T1/3] range, the platform surges in the positive X-direction, causing the blade's movement to align with the incoming wind, which reduces the actual inflow wind speed. Consequently, the blade's angle of attack is lower than in the [0, T1/3] range, explaining why the torque peak of Blade 1 decreases progressively across these three cycles.

During this same period, the platform undergoes negative pitching, with the pitch angle decreasing from its maximum back to 0°. For the original floating VAWT, the pitch angle drops from 2.5° to 0°, while for the VAL-structured floating VAWT, it decreases from 2.0° to 0°. The faster rate of pitch reduction in the original floating VAWT leads to a stronger interaction between the blades and the incoming wind, mitigating the torque reduction caused by the platform's positive surge. As a result, the torque peak for the VAL-structured floating VAWT is lower than that of the original floating VAWT during this period.

This demonstrates that the torque of the floating VAWT is significantly influenced by the platform's surge and pitch responses. While the VAL structure, by notably improving the platform's pitch response, may reduce the beneficial interaction between blade motion and wind speed at certain moments, it overall lessens the interaction between the blades and the incoming wind. This ultimately helps to mitigate the issue of large fluctuations in the power coefficient of the floating VAWT.

5.2.4. *Mooring lines tension*

The time-varying mooring line tension curves for the original floating VAWT and the floating VAWT with the VAL structure are shown in Fig. 32.

It can first be observed that the tension in mooring line C2 is consistently higher than in C1 and C3 throughout the entire time period. This is mainly because C2 is on the windward side, and as the floating VAWT shifts its average equilibrium position in the positive X-direction

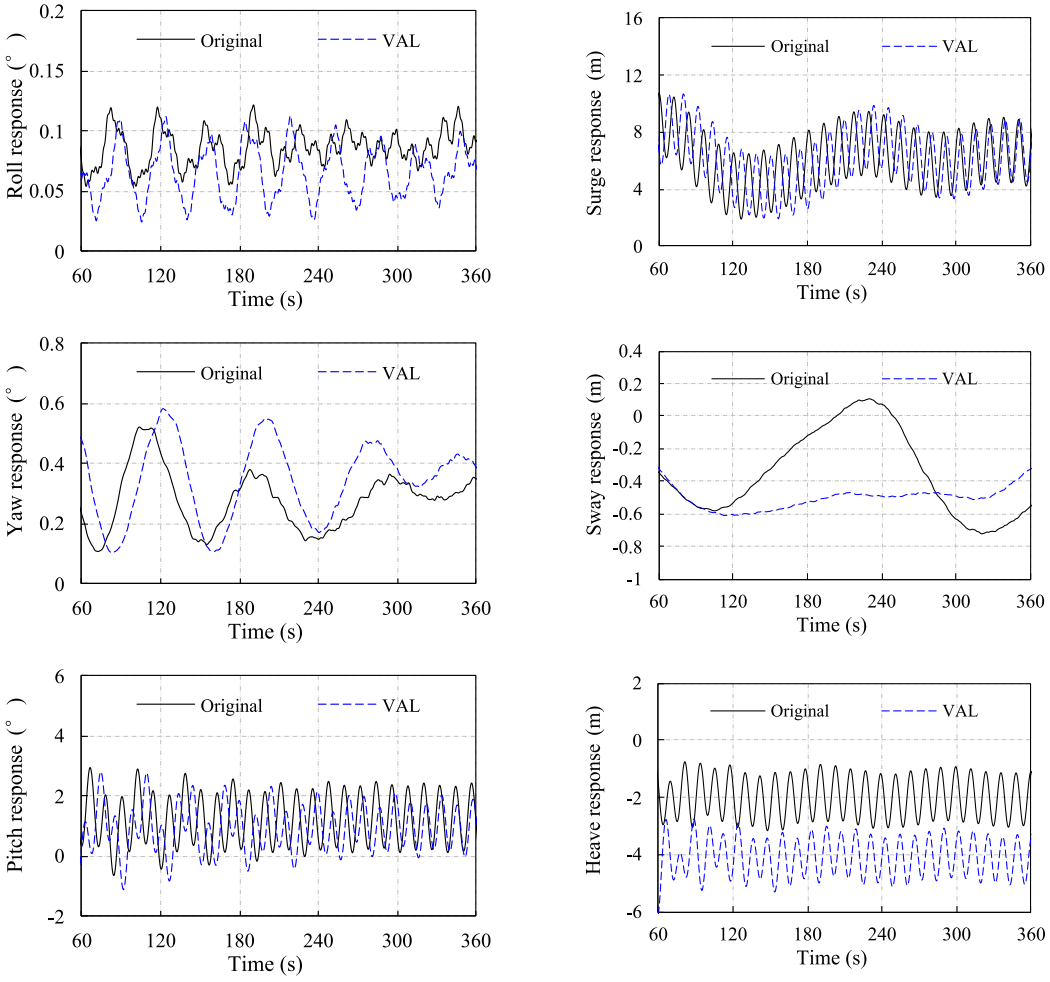

Fig. 29. Six-DOF response of the floating VAWT with and without VA configuration.

Table 12
Statistical values of surge, pitch and heave responses of the floating VAWT with and without VA configuration.

		Maximum value	Minimum value	Fluctuation amplitude	Standard deviation
Surge	Original	9.04 m	3.79 m	5.25 m	1.61 m
	VAL	8.94 m	4.35 m	4.59 m	1.54 m
Pitch	Original	2.43 °	0.09 °	2.33 °	0.79 °
	VAL	2.03 °	−0.01 °	2.04 °	0.61 °
Heave	Original	−0.94 m	−3.04 m	2.09 m	0.68 m
	VAL	−3.11 m	−5.03 m	1.92 m	0.62 m

due to wind and wave loads, C2 becomes more tensioned compared to C1 and C3, resulting in higher tension.

The mooring line tension curves for the floating VAWT with the VAL structure follow a similar trend to the original floating VAWT, both showing clear periodic fluctuations. Additionally, the VAL structure significantly reduces the tension in C1 and C3, which is primarily due to its ability to improve the platform's surge and pitch responses, thereby reducing the lateral movement and tilting of the platform that would otherwise affect the moorings.

It's important to note that for a individual platform, the VAL structure increases the surge average equilibrium position, shifting it backward, which lengthens the slack in C1 and C3 but increases the tension in C2. However, for the entire floating VAWT system, the VAL structure

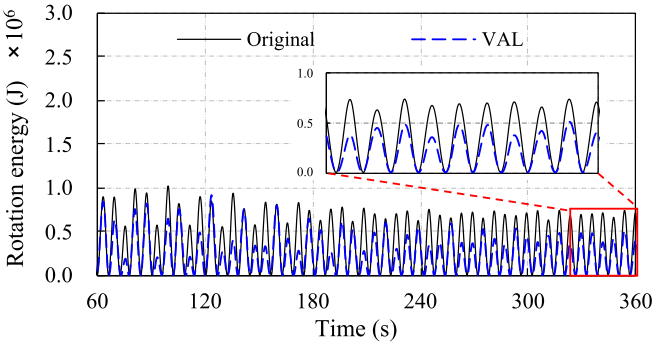

Fig. 30. Time history of rotational energy for the floating VAWT with and without VA configuration.

reduces both the surge response amplitude and the average equilibrium position, preventing a significant increase in C2 tension. This further demonstrates that the VAL structure enhances the mooring safety factors of the floating VAWT, ensuring safe and stable operation.

6. Conclusions

This study introduces a novel nature-inspired design based on OC4 semi-submersible platform, drawing inspiration from the unique leaf

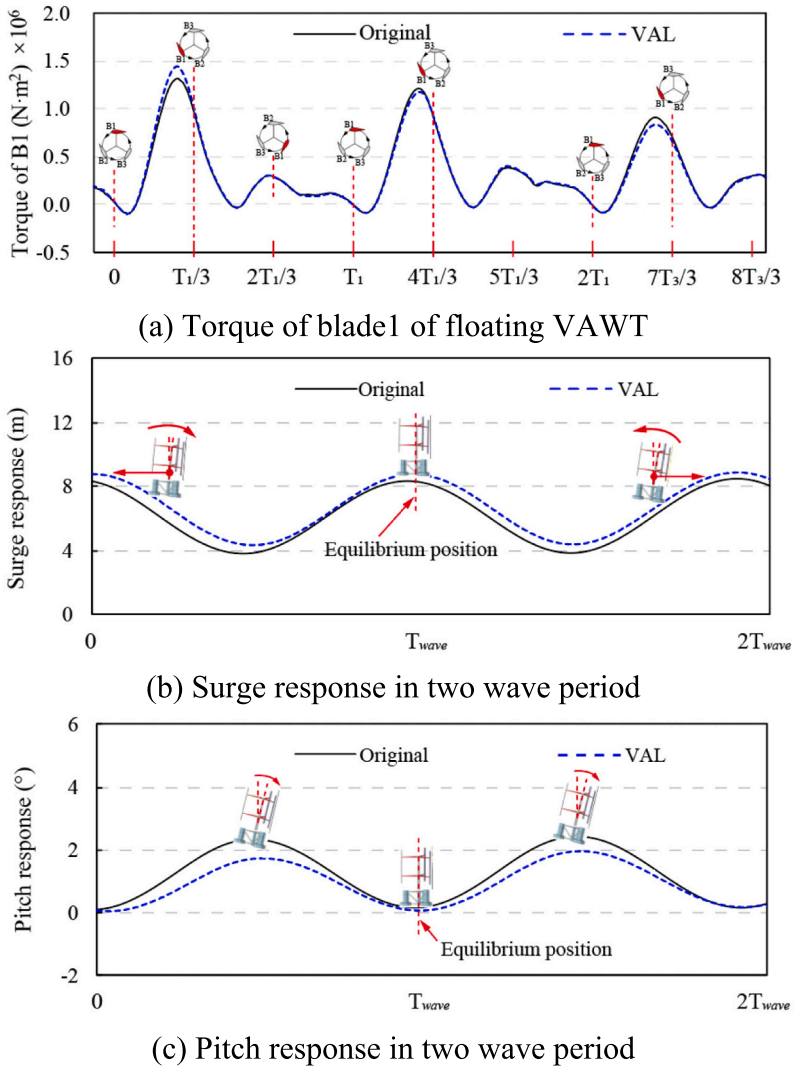

Fig. 31. Torque of a blade1 of the floating VAWT and pitch and surge responses over the same time period.

venation structure of the *Victoria Amazonica* (VA). The goal is to address the significant fluctuations in the power coefficient of floating VAWTs through enhance platform stability. Numerical simulations were conducted using the commercial CFD software STAR-CCM+ to perform coupled aero-hydro dynamic calculations for the individual platform and floating VAWT. The RANS based SST k-ω turbulence model was used to resolve the turbulent flow field, while the DFBI model was applied to simulate the free motion response of the floating system. The VOF wave model was employed to simulate surface gravity waves at the air-water interface, and regular waves were modeled using the fifth-order approximation of Stokes wave theory. The accuracy of the aerodynamic and hydrodynamic models was validated separately using small-scale VAWT wind tunnel experiments and free decay tests in a wave basin.

In the Grasshopper visual programming environment within Rhino, a parametric model of the VA leaf venation structure, including the main veins, branches, and ribs, was developed. The shape and dimensions of the leaf vein curves were optimized using voxel manipulation functions from the Grasshopper plugin Dendro. By adjusting the number of concentric circles, bio-inspired structural configurations with different vein levels (VAL, VAM, and VAS) were created, enabling numerical modeling of both the individual platform and the floating VAWT system incorporating these novel designs. The main conclusions from the analysis of the aero-hydro dynamic performance of the three VA configurations on both the individual platform and the integral floating VAWT system are as follows:

(1) The VA structure significantly improves the hydrodynamic performance of the individual platform, especially in the surge, pitch, and heave DOF. The stabilizing effect increases with the leaf venation level, with the VAL configuration reducing pitch amplitude by up to 38 % compared to the original platform, significantly improving tilt resistance. Furthermore, the VA structures cause a slight forward shift in the surge equilibrium position of platform but reduce surge response amplitude. Due to the VA structure's internal chambers, the VA platforms have a reduced displaced volume and slightly lower buoyancy, resulting in a lower draft than the original platform. However, heave response amplitude and standard deviation are also reduced. The VA structure ensures that mooring line (C1–C3) tensions remain with high safety factor, although C2 tension is slightly elevated due to the forward shift in the surge equilibrium position.

(2) When applied to the integral floating VAWT system, the VA structure's effect on surge differs from that observed in the individual platform. The VA structure does not cause a significant backward shift in the overall equilibrium position for the entire floating VAWT system. Instead, the VAL structure reduces both the surge response amplitude and the average equilibrium

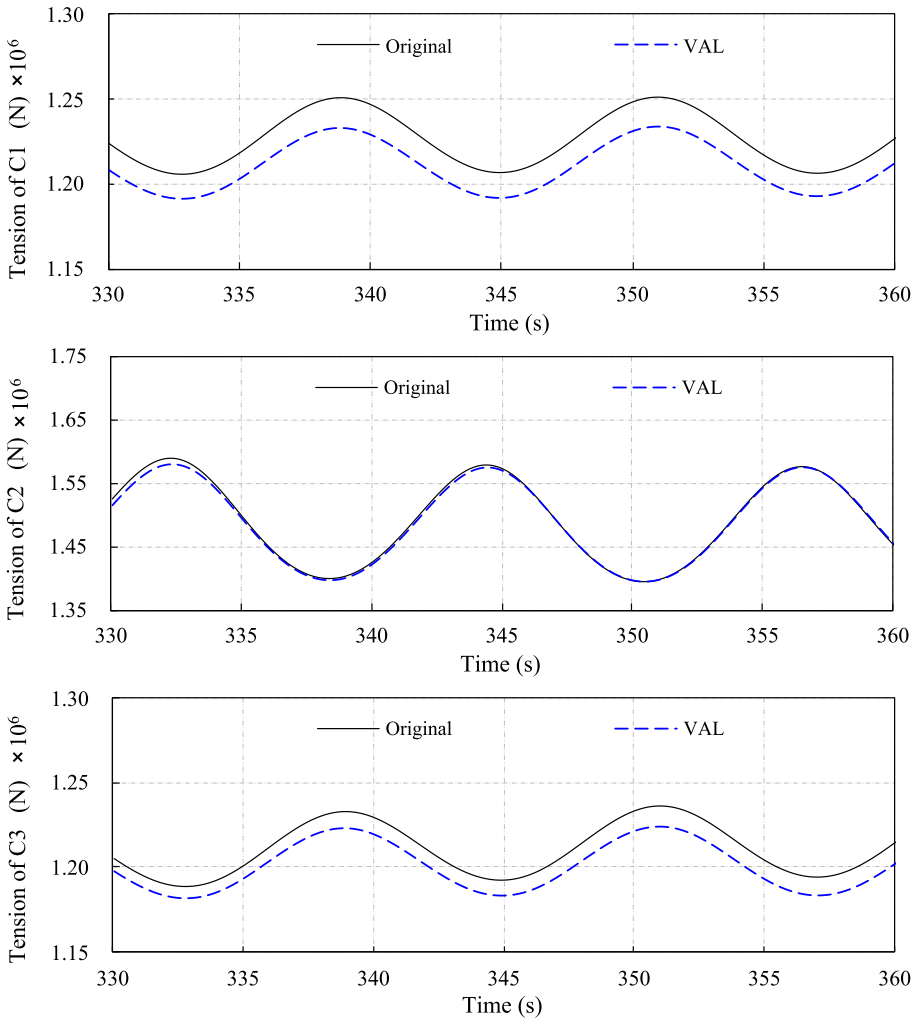

Fig. 32. Mooring lines tension for floating VAWT with and without VA configuration.

position, preventing a significant increase in C2 tension. This demonstrates that the VAL structure can enhance the mooring safety factors of the floating VAWT, ensuring safe and stable operation.

(3) The primary physical mechanism by which the VA structure increases platform stability lies in its internal chambers, which increase shear and centrifugal forces within the fluid, promoting vortex formation. The VA structure's chambers increase the contact area between the fluid and chamber walls, amplifying viscous effects. Viscosity is the main driver of vortex generation, and the increased wall interactions significantly raise vortex density. These vortices interact with the chamber walls, effectively dissipating wave energy by converting it to heat, thus achieving effective wave energy absorption.

(4) By reducing the platform's dynamic response (surge, pitch, and heave), the VA structure reduces interactions between the VAWT blades and the incoming flow, thereby mitigating alternating torque peaks on the windward side. This reduces the standard deviation of power coefficient fluctuations, contributing to more stable power generation in floating VAWTs.

(5) While this study finds that higher leaf venation levels (VAL) provide optimal stabilization and reduction in power coefficient fluctuations, increasing the leaf venation level indefinitely is not advisable in practical applications. Higher venation levels may lead to increased draft and platform mass, which can compromise overall performance. Additionally, as the leaf venation level increases, the internal chamber volume decreases, eventually reducing vortex capture capability and hindering effective kinetic energy dissipation.

Future studies could further investigate the fluid-structure interaction of the VA structure, focusing on load resistance, structural strength, and fatigue life under extreme sea conditions. Overall, this bio-inspired platform design has significant potential for the next generation of floating platforms. While construction and implementation currently pose challenges, advancements in 3D printing and CNC manufacturing, along with the use of advanced materials and modular assembly techniques, may enable cost-effective production with reduced material use, making VA platforms a promising option for practical engineering applications in the future.

CRediT authorship contribution statement

Qingsong Liu: Writing – original draft, Visualization, Validation, Methodology, Investigation. **Musa Bashir:** Writing – review & editing, Writing – original draft, Supervision, Methodology, Funding acquisition. **Haoda Huang:** Visualization, Validation, Methodology. **Weipao Miao:** Visualization, Methodology, Investigation, Conceptualization. **Zifei Xu:** Writing – review & editing, Visualization, Methodology. **Minnan Yue:** Writing – review & editing, Resources, Conceptualization. **Chun Li:** Writing – review & editing, Funding acquisition, Conceptualization.

Declaration of competing interest

The authors declare that they have no known competing financial interests or personal relationships that could have appeared to influence the work reported in this paper.

Acknowledgements

This research is partially funded by UKRI Innovate UK under grant numbers TS/Y006364/1, TS/Y005236/1, and TS/X018407/1. The authors gratefully acknowledge the support of the High-Performance Computer Cluster-Prospero at LJMU, which generously provided the computational resources essential for this research.

Data availability

No data was used for the research described in the article.

References

[1] Global Wind Energy Council. Global wind report 2024. Brussels: GWEC; 2024.
[2] Global Wind Energy Council. Global offshore wind report 2024. Brussels: GWEC; 2024.
[3] Bagalkot N, Jose J, Keprate A. Chapter 2 - key components of the horizontal axis wind turbine. Multiphysics of Wind Turbines in Extreme Loading Conditions 2024:17–31.
[4] Arapogianni A, Genachte A, Ochagavia R, et al. Deep water: The next step for offshore wind energy. Brussels: European Wind Energy Association; 2013.
[5] McAuliffe FD, Judge FM, Murphy J. Modelling the installation of next generation floating offshore wind farms. Appl Energy 2024;374:124001.
[6] Subbulakshmi A, Verma M, Keerthana M, et al. Recent advances in experimental and numerical methods for dynamic analysis of floating offshore wind turbines - an integrated review. Renew Sustain Energy Rev 2022;164:112525.
[7] Cheng ZS. Integrated dynamic analysis of Floating vertical Axis wind turbines. Trondheim: Norwegian University of Science and Technology; 2016.
[8] Jonkman J. Definition of the Floating system for phase IV of OC3. United States: Office of Scientific and Technical Information Reports; 2010.
[9] Robertson A, Jonkman J, Masciola M, et al. Definition of the semisubmersible Floating system for phase II of OC4. United States: Office of Scientific and Technical Information Reports; 2014.
[10] Bachynski E, Moan T. Design considerations for tension leg platform wind turbines. Marine Structures 2012;29(1):89–114.
[11] Deep Water. The next step for offshore wind energy. European Wind Energy Association; 2013. Tech. Rep.,.
[12] Energyfacts. Lifting of the World's Biggest Nacelle, Haliade-X 12MW. https://www.energyfacts.eu/lifting-of-the-worlds-biggest-nacelle-haliade-x-12-mw/;; 2019. accessed 18 March 2024.
[13] Stehly T, Duffy P, Mulas Hernando D. 2022 cost of wind energy Review. Golden: National Renewable Energy Laboratory; 2022.
[14] Ghigo A, Faraggiana E, Giorgi G, et al. Floating vertical Axis wind turbines for offshore applications among potentialities and challenges: a review. Renew Sustain Energy Rev 2024;193:114302.
[15] Aslam Bhutta M, Hayat N, Farooq A, et al. Vertical axis wind turbine – a review of various configurations and design techniques. Renew Sustain Energy Rev 2012;16(4):1926–39.
[16] Borg M, Collu M, Kolios A. Offshore floating vertical axis wind turbines, dynamics modelling state of the art. Part II: mooring line and structural dynamics. Renew Sustain Energy Rev 2014;39:1226–34.
[17] Gipe P. Wind energy basics: A guide to home and community-scale wind-energy systems. Chelsea Green Publishing; 2009.
[18] Sutherland HJ, Berg DE, Ashwill TD. A retrospective of VAWT technology. Tech. Report SAND2012-0304,. Albuquerque, New Mexico, USA: Sandia National Laboratories; 2012.
[19] Vita L. Offshore vertical Axis wind turbine with Floating and rotating foundation. Technical University of Denmark; 2011.
[20] Future Deep Sea Wind Turbine Technologies. Final Report Summary-DEEPWIND. https://cordis.europa.eu/project/id/256769/reporting;; 2024. accessed 19 April 2024.
[21] Deep-water vertical-axis wind turbine gets last dry run. https://www.rechargenews.com/technology/deep-water-vertical-axis-wind-turbine-gets-last-dry-run/1-1-841194;; 2016. accessed 19 April 2024.
[22] Bybee Karen. Use of a vertical wind turbine in an offshore Floating wind farm. J Petrol Tech 2011;63(07):105–7.
[23] Floating Gyro-Stabilized VAWT to Be Tested in Norway (VIDEO). https://www.offshore-energy.biz/floating-gyro-stabilized-vawt-to-be-tested-in-norway-video/;; 2013. accessed 19 April 2024.
[24] A Potential Breakthrough in Offshore Wind Power. https://www.fastcompany.com/1661980/a-potential-breakthrough-in-offshore-wind-power;; 2010. accessed 19 April 2024.
[25] Andrew S. Design optimisation of an offshore vertical axis wind turbine. Energy 2013;166:7–18.
[26] After Fukushima, a glut of green energy in Japan. https://www.cbsnews.com/news/after-fukushima-a-glut-of-green-energy-in-japan/;; 2022. accessed 19 April 2024.
[27] 1-MW floating vertical axis wind turbine to be deployed off Norway. https://newatlas.com/energy/seatwirl-vawt-norway/;; 2022. accessed 19 April 2024.
[28] Parneix N, Fuchs R, Immas A, et al. Efficiency improvement of vertical-axis wind turbines with counter-rotating lay-out. 2016. p. 1–7.
[29] SeaTwirl to install 1 MW floating vertical-axis wind turbine in Norway. https://www.inceptivemind.com/seatwirl-install-1-mw-floating-vertical-axis-wind-turbine-norway/27413/; 2022. accessed 19 April 2024.
[30] Borg M, Collu M. A comparison between the dynamics of horizontal and vertical axis offshore floating wind turbines. Philosophical Transactions of the Royal Society A 2015;373(2035):20140076.
[31] Liu Q, Bashir M, Iglesias G, Miao W, Yue M, Xu Z, et al. Investigation of aero-hydro-elastic-mooring behavior of a H-type floating vertical axis wind turbine using coupled CFD-FEM method. Appl Energy 2024;372:123816.
[32] Han YQ, Le CH, Ding HY, et al. Stability and dynamic response analysis of a submerged tension leg platform for offshore wind turbines. Ocean Eng 2017;129:68–82.
[33] Zhang HJ, Wang H, Cai X, et al. Research on the dynamic performance of a novel floating offshore wind turbine considering the fully-coupled-effect of the system. Journal of Marine Science and Engineering 2022;10(3):341.
[34] Bashetty S, Ozcelik S. Design and stability analysis of an offshore floating multi-wind turbine platform. Inventions 2022;7(3):58.
[35] Shen Y, Liu CY, Pan WC, et al. Design and fully coupled dynamic response analysis of a new floating offshore wind platform. Journal of Marine Science and Engineering 2023;11(7):1368.
[36] Yang Y, Bashir M, Michailides C, et al. Development and application of an aero-hydro-servo-elastic coupling framework for analysis of floating offshore wind turbines. Renew Energy 2020;161:606–25.
[37] Ding QW, Li C, Yu NT, et al. Numerical and experimental investigation into the dynamic response of a floating wind turbine spar array platform. Journal of Mechanical Science and Technology 2018;32:1106–16.
[38] Ding QW, Li C. Research on the influence of helical strakes on dynamic response of floating wind turbine platform. China Ocean Engineering 2017;31(2):131–40.
[39] Yang WX, Tian WY, Hvalbye O, et al. Experimental research for stabilizing offshore Floating wind turbines. Energies 2019;12(10):1947.
[40] Yue MN, Liu QS, Li C, et al. Effects of heave plate on dynamic response of floating wind turbine spar platform under the coupling effect of wind and wave. Ocean Eng 2020;201:107103.
[41] Yao YS, Ning DZ, Deng SJ, et al. Hydrodynamic investigation on floating offshore wind turbine platform integrated with porous shell. Energies 2023;16(11):4376.
[42] Wakui T, Nagamura A, Yokoyama R. Stabilization of power output and platform motion of a floating offshore wind turbine-generator system using model predictive control based on previewed disturbances. Renew Energy 2021;173:105–27.
[43] Box F, Erlich A, Guan JH, et al. Gigantic floating leaves occupy a large surface area at an economical material cost. Sci Adv 2022;8(6):1–7.
[44] Brebbia CA, Carpi A. Design and nature V: comparing Design in Nature with science and engineering. WIT Transactions on Ecology and the Environment 2010:411–3.
[45] Eurasia Review. New Research Solves Crystal Palace Mystery. https://www.eurasiareview.com/17092024-new-research-solves-crystal-palace-mystery/;; 2024. accessed 2 November 2024.
[46] So Transparent. London's iconic Crystal Palace reloaded – Part I. https://www.architonic.com/en/story/selected-by-materials-council-so-transparent-london-s-iconic-crystal-palace-reloaded-part-i/7000931;; 2014. accessed 2 November 2024.
[47] Meriam JL, Kraige LG. Engineering Mechanics dynamics. 7th ed. Virginia: Virginia Polytechnic Institute and State University; 2012.
[48] Idema T. Mechanics and relativity. Netherlands: Delft University of Technology; 2024.
[49] Prosperetti A, Tryggvason G. Computational methods for multiphase flow. Cambridge: Cambridge University Press. 2007.
[50] Fenton John D. A fifth-order stokes theory for steady waves. Journal of waterway port coastal and ocean Engineering111; 1985. p. 216–34. 2.
[51] Veritas DN. Environmental conditions and environmental loads, recommended practice DNV-RP-C205. 2007.
[52] Choi J, Yoon SB. Numerical simulations using momentum source wave-maker applied to RANS equation model. Coastal Engineering 2009;56:1043–60.
[53] Love AEH. A treatise on the mathematical theory of elasticity. 4th ed. New York: Dover Publications Inc; 2003.
[54] WeWantToLearn.net. Fractal branching in the *Victoria Amazonica*. https://wewanttolearn.wordpress.com/2020/01/23/fractal-branching-in-the-victoria-amazonica/;; 2020. accessed 13 November 2023.
[55] Rian LM, Asayama S. Computational design of a nature-inspired architectural structure using the concepts of self-similar and random fractals. Automation in Construction 2016;66:43–58.
[56] Menter FR. Zonal two equation k-w turbulence models for aerodynamic flows. In: 23rd fluid dynamics, Plasmadynamics, and lasers conference, Orlando; 1993.
[57] Radhakrishnan J, Sridhar S, Zuber M, et al. Design optimization of a contra-rotating VAWT: a comprehensive study using Taguchi method and CFD. Energ Conver Manage 2023;2023(298):117766.
[58] Kouaissah O, Franchina N, Siddiqui MS, et al. A computational study on the performance and wake development of a tilted H-Shaped VAWT rotor. Renewable Energy 2024;222:119932.

[59] Battist L, Persico G, Dossena V, et al. Experimental benchmark data for H-shaped and troposkien VAWT architectures. Renew Energy 2018;125:425–44.
[60] Coulling AJ, Goupee AJ, Robertson AN, et al. Validation of a FAST semi-submersible floating wind turbine numerical model with DeepCwind test data. Journal of Renewable and Sustainable Energy 2013;5:023116.
[61] Cheng P, Huang Y, Wan DC. A numerical model for fully coupled aero-hydrodynamic analysis of floating offshore wind turbine. Ocean Eng 2019;173:183–96.
[62] Tran TT, Kim DH. Fully coupled aero-hydrodynamic analysis of a semi-submersible FOWT using a dynamic fluid body interaction approach. Renew Energy 2016;92:244–61.
[63] Cheng P, Huang Y, Wan DC. A numerical model for fully coupled aero-hydrodynamic analysis of floating offshore wind turbine. Ocean Eng 2019;173:183–96.
[64] American Petroleum Institute. Recommended practice for design. Manufacture: Installation, and Maintenance of Synthetic Fiber Ropes for Offshore Mooring, Boston; 2001.